1991ApJS...76.1127V

THE ASTROPHYSICAL JOURNAL SUPPLEMENT SERIES, 76:1127–1167, 1991 August
© 1991. The American Astronomical Society. All rights reserved. Printed in U.S.A.

THE *EINSTEIN* OBJECTIVE GRATING SPECTROMETER SURVEY OF GALACTIC BINARY X-RAY SOURCES

S. D. VRTILEK, J. E. MCCLINTOCK, AND F. D. SEWARD
Harvard-Smithsonian Center for Astrophysics, 60 Garden Street, Cambridge, MA 02138

AND

S. M. KAHN AND B. J. WARGELIN
Department of Physics, University of California at Berkeley, Berkeley, CA 94720
Received 1990 November 5; accepted 1991 January 31

ABSTRACT

The results of observations of 22 bright Galactic X-ray point sources taken with the Objective Grating Spectrometer (OGS) of the *Einstein Observatory* are presented. In most cases simultaneous observations with the Monitor Proportional Counter (MPC) are available also. By combining the high spectral resolution data from the OGS ($E/\Delta E = 31[E(\mathrm{keV})]^{-1}$ over the range 0.2–1.5 keV), which effectively constrain column densities, with the higher energy range data from the MPC (1–20 keV), which serve to constrain continuum temperatures, the most reliable measurements to date of X-ray column densities to these sources have been derived. The measured column densities range from $N_{\mathrm{H}} = 4.0 \times 10^{19}$ to 5.0×10^{23} cm^{-2}. The extinction $A_v^{\text{X-ray}}$ implied by measured N_{H} is always greater than or approximately equal to optically measured A_v^{opt}; in addition, for several sources where multiple observations exist, the column density varies as a function of orbital phase. These results are consistent with the idea that some of the objects have a component of column density intrinsic to the source in addition to an interstellar component.

The K-edge absorption due to oxygen is clearly detected in 10 of the sources, and the Fe L and Ne K edges are detected in a few. X-ray line emission is detected unambiguously in 11 of the sources and marginally in another four; the line features observed suggest that the emitting material spans a large range in temperature and ionization state. Neither models with excitation by photoionization nor those with excitation by collisions can reproduce the relative intensities of the features. However, features that can be associated with one or the other mechanisms are observed simultaneously; since X-ray binaries are not spatially resolved, it is probable that emission originating in a collisionally excited (coronal) region and emission from a photoionized region excited directly by the central source are combined in the spectra that we have obtained. Future missions with higher energy resolution and sensitivity will greatly facilitate measurement of line velocities as a function of binary phase, enabling disentanglement of the line emission regions.

An atlas of the raw count spectrum and photon spectrum of each observation is presented.

Subject headings: X-rays: binaries — X-rays: spectra

1. INTRODUCTION

The Objective Grating Spectrometer (OGS) on the *Einstein Observatory* had as its primary objective the detection of sharp features (emission and absorption lines and absorption edges) in the soft X-ray spectra of celestial sources (Dijkstra, Lantwaard, & Timmerman 1978). The OGS is the highest resolution X-ray instrument with a broad energy range yet flown on a satellite.[1] Because of its modest effective area, the OGS was most useful for observations of the brightest celestial X-ray sources, namely Galactic X-ray binaries. This study presents the results from a uniform analysis of all the X-ray binaries observed by the OGS. In total 22 sources were observed; a few were observed several times, allowing us to follow changes in spectral behavior with binary phase.

[1] The Focal Plane Crystal Spectrometer (FPCS) on *Einstein* had much higher resolution but a very narrow bandwidth (Canizares et al. 1979), and the Transmission Grating Spectrometer (TGS) on *EXOSAT* had 3–5 times lower spectral resolution (Chiappetti et al. 1990; Osborne et al. 1986).

The discovery in 1971 of X-ray pulsations from two Galactic sources, Cen X-3 and Her X-1 (Schreier et al. 1972; Tananbaum et al. 1972), gave birth to the standard model for accreting binary X-ray sources: Doppler-shift analysis of the pulsations established that the sources were located in binary systems; the application of well-understood binary orbital mechanics to the X-ray and optical data provided precise determinations of the orbital parameters and constraints on the sizes and masses of the system components; the high X-ray luminosities, rapid X-ray variability, and high masses deduced for the X-ray emitting components quickly led to the conclusion that they must be some form of compact object. The "classic" X-ray binary is a system composed of an accreting neutron star (or occasionally a black hole) and a "normal" star. X-ray binaries are commonly subdivided according to the mass of the normal star: systems with massive ($>10\ M_\odot$) O or B stars, and systems with low-mass ($<1\ M_\odot$) stars (Bradt & McClintock 1983, hereafter BMC83).

The high-mass X-ray binaries (HMXBs) contain massive early-type stars with short lifetimes ($<10^7$ yr). The optical fluxes are high, giving X-ray–to–optical luminosity ratios in

© American Astronomical Society • Provided by the NASA Astrophysics Data System

1991ApJS...76.1127V

the range 10^{-5} to 10. More than half of the HMXBs exhibit regular X-ray pulsations with periods from 0.1 to 1000 s, attributed to rotation of a highly magnetized (10^{12} G) neutron star. Doppler studies of the X-ray pulsations, timing of X-ray eclipses, and optical radial velocity studies have yielded accurate determination of the masses of the components for several systems (Rappaport & Joss 1983; Bahcall 1978).

In contrast, the low-mass X-ray binaries (LMXBs) contain faint optical companions with long lifetimes of 10^8–10^9 yr (but for a dissenting view, see Ruderman et al. 1989). The optical light is due predominantly to X-ray heating of the accretion disk, a process that gives X-ray–to–optical luminosity ratios from 10 to 10^4. With two exceptions (4U 1626−67; 4U 1728−24), no high-Q pulsations are seen. The lack of coherent pulsations and the presence of bursts in X-ray intensity attributed to thermonuclear burning on the surface of the neutron star imply that LMXBs have relatively weak magnetic fields ($\lesssim 10^{10}$ G) (Lewin & Joss 1983). In 1985, the discovery of rapid quasi-periodic oscillations (QPOs) in the X-ray emission from LMXBs sparked a new interest in these sources: it is thought that the QPOs may provide a link between LMXBs and the millisecond pulsars, a link which has been implied by evolutionary theories of binary pulsars for some time (Hasinger et al. 1985; van der Klis et al. 1985).

The continuum models used to fit the X-ray spectra of X-ray binaries are not unique, in part because of limitations of the observing instruments (Vacca et al. 1987; Vrtilek, Swank, & Kallman 1988, hereafter VSK88; Ponman, Foster, & Ross 1990, hereafter PFR90); the parameters derived from such models are not reliable descriptors of the spectra. Instead, X-ray color-color diagrams have gained currency for the more instrument-independent "spectral signatures" which they can provide. Such a diagram is constructed by forming intensity ratios of three X-ray energy bands. The hard color (high energy band/medium energy band) tends to be sensitive to temperature changes and the soft color (medium energy band/low energy band) sensitive to absorption effects. Thus the two together should reflect "intrinsic" properties of the system which are unaffected by changes in the geometry of the emitting region; plotting the hard color against the soft color is an X-ray analog of the color-color (e.g., $U-B$, $B-V$) diagrams of optical astronomy (Lamb 1989). In such diagrams, each HMXB forms a distinct point (if one excludes the eclipse and any pre-eclipse dips), implying that the X-ray flux in all three bands change simultaneously so that HMXB always have the same color ratio (Belloni & Hasinger 1990). The LMXBs, on the other hand, show two distinct classes: the "Z-sources" form a Z-shaped curve with distinct spectral and temporal behavior in each branch of the Z, and the "atoll" sources show little correlated behavior between the colors.

The lack of uniqueness among the models that give satisfactory fits to the X-ray continuum spectra suggests that current interpretations involving complex models may lack physical significance. Accordingly, other evidence, independent of spectral continuum fitting, such as that from spectral lines, must provide additional constraints for future models. The influence of spectral lines on model fits of the continuum was demonstrated in a study of nine *Einstein* Solid State Spectrometer (SSS) observations of five Galactic binary X-ray sources for which OGS data exist: VSK88 showed that the goodness of fit of simple models to SSS data is greatly improved by adding line features identified in the OGS to the models. The SSS, with a constant energy resolution of 200 eV across its 1–4.5 keV bandpass, cannot resolve the lines but is nonetheless influenced by their presence.

The OGS observations provide the most reliable measurements yet obtained of column densities to X-ray binaries as well as measurements of absorption edges and absorption and emission lines. The detection of spectral features is an important part of this survey because they have the potential for use as new diagnostics of plasma conditions in and around binary systems (Liedahl et al. 1990). Ultimately, the study of line emission at high spectral resolution will be able to provide detailed information on temperatures, densities, and excitation conditions, as well as on geometries and kinematics of the systems being observed. The OGS has a small fraction of the resolution and efficiency of future grating instruments, yet it has already demonstrated the importance of sharp spectral features to our understanding of X-ray binaries and given impetus to studies that model X-ray line emission from hot plasmas (Liedahl et al. 1990; Kallman et al. 1991; Kallman, Vrtilek, & Kahn 1989, hereafter KVK89). These results give a foretaste of the data that will become available from the next major space missions such as AXAF and XMM, both of which will be equipped with high-resolution X-ray spectrometers (Brinkman et al. 1987; Canizares et al. 1987).

In § 2 the instruments and observations are discussed, and in § 3 data reduction techniques and results. Comments on several individual sources are presented in § 4. Section 5 presents conclusions and discusses implications of these results for models of X-ray binaries.

2. INSTRUMENTS AND OBSERVATIONS

A list of all observations of X-ray binaries made with the OGS, including the times at which they were taken and the source exposure for the *Einstein* Monitor Proportional Counter (MPC) and the OGS, is given in Table 1. The 4U designations of the X-ray sources, their common X-ray names, and the names of known optical counterparts are listed in the first column. The distribution in Galactic coordinates of the sources used in this study is shown in Figure 1. The source classifications are taken from BMC83 with the exception of Her X-1, which we list as an intermediate mass system (IMXB). We analyzed a total of 2.9×10^5 s net source exposure from the OGS and 1.9×10^5 s net source exposure time from the MPC (after removal of data gaps due to earth occultations, South Atlantic Anomaly passage, and other causes). The *Einstein* OGS data comprise 28 separate observations of the 22 sources taken with the 1000 lines mm^{-1} grating, and four observations (three of Her X-1 and one of V801 Ara) taken with the 500 lines mm^{-1} grating. For three sources (Her X-1, Cyg X-2, and 1820−30) the observation intervals were subdivided into a few shorter intervals because the source changed its behavior markedly during the observation. Simultaneous observations with the MPC were available for all but one source, the very bright source Sco X-1, which saturated the MPC telemetry system.

The OGS has been described in detail by Seward et al. (1982, hereafter S82), Mewe et al. (1982), and Kahn, Seward, &

© American Astronomical Society • Provided by the NASA Astrophysics Data System

1991ApJS...76.1127V

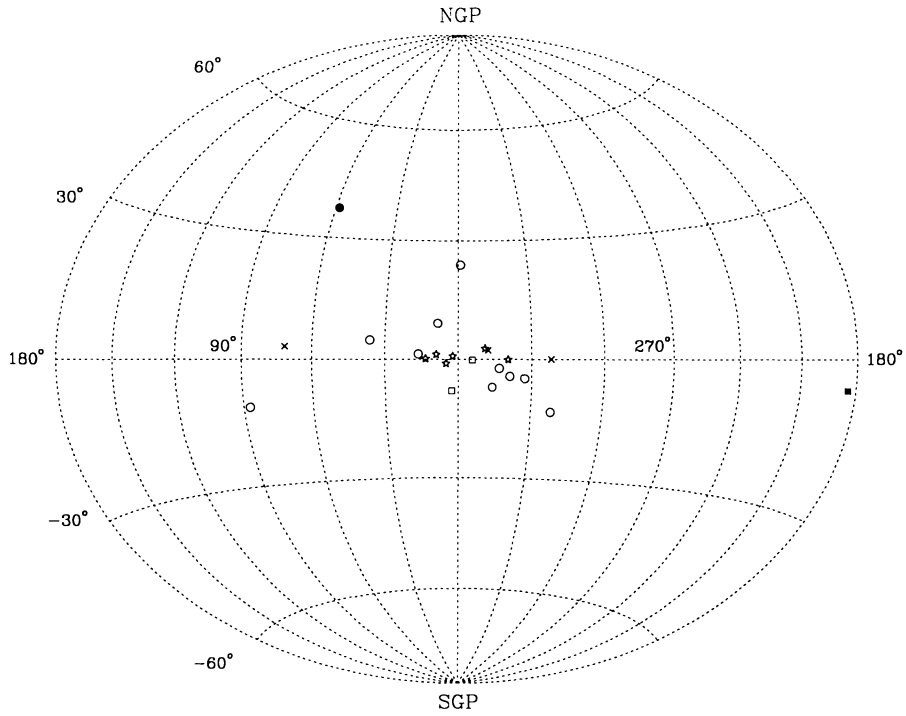

FIG. 1.—Distribution in Galactic latitude and longitude of the 22 sources observed in this study. The different symbols designate massive (*crosses*), low-mass (*open circles*), intermediate-mass (*filled circles*), globular cluster (*open squares*), and optically unidentified sources (*stars*). The filled square represents the Crab Nebula which was used to test the joint MPC+OGS analysis system.

Chlebowski (1984, hereafter KSC84). It consisted of two transmission gratings, either of which could be placed in the X-ray path at the mirror exit. For the 1000 lines mm^{-1} grating, the dispersion was 0.0312 Å per pixel on the High Resolution Imager (HRI; Henry et al. 1977). The assembled telescope with detectors and gratings was calibrated in a vacuum tank before flight. The grating response was measured with a continuum source and with beams of characteristic K or L X-ray lines at 10 energies. The line measurements established the energy scale and response giving for the 1000 lines mm^{-1} grating a resolution of $E/\Delta E = 31E(\mathrm{keV})^{-1}$ or a constant 0.4 Å over an energy range of 0.2–2.0 keV; and for the 500 lines mm^{-1} grating a resolution $E/\Delta E = 16E(\mathrm{keV})^{-1}$, or a constant 0.8 Å over an energy range of 0.1–1.5 keV.

Both line and continuum sources verified that the first-order diffraction response on either side of the zero order was the same. The two first orders may thus be added. The continuum source revealed sharp discontinuities at 43.7 Å and 14.5 Å which are ascribed to absorption edges from the carbon in the parylene coating on the 1000 lines mm^{-1} grating and in the HRI UV filter and from the Ni coating on the mirror, respectively. There were no other instrumental peculiarities which might appear as spectral features: the instrument was "well behaved" to the level of sensitivity of the observations presented. To the best of our knowledge, there are no other sources in the HRI fields for any of the OGS observations presented which might appear as emission lines because they accidentally lie in the dispersed spectrum.

An in-flight observation of the Crab Nebula was used to calibrate the 1000 lines mm^{-1} grating. Because the Crab is an extended source, a direct deconvolution technique similar to the one described by Kahn & Blisset (1980) was used to determine its spectrum (Kahn & Seward 1982). The deconvolved Crab spectrum clearly showed the presence of a strong oxygen K-edge. Using the deconvolved spectrum of the Crab, the efficiency of the grating between 0.3 and 1.0 keV was adjusted to obtain agreement with the previously established spectrum (a power law with photon index -2.08 ± 0.05 [Toor & Seward 1974], and a neutral hydrogen column density of $3.1 \pm 0.2 \times 10^{21}$ cm^{-2} [Charles et al. 1979]), using the interstellar absorption coefficients of Brown & Gould (1970). No adjustment was made to the normalization. The efficiency of the 500 lines mm^{-1} grating was calibrated using preflight data below 0.28 keV and above 0.5 keV and using in-flight observations of Her X-1 between 0.28–0.5 keV; continuity was required at 0.5 keV (S82). The effective areas of the gratings as used in this study are shown in Figure 2.

The MPC was a collimated proportional counter detector filled with argon and carbon dioxide. It had a square field of view, 1.5° FWHM, which was co-aligned with the telescope. A 1.5 mil Be window sealed the gas in the detector and shielded the detector from ultraviolet radiation. The characteristics of the MPC have been described in detail by Gaillarditz et al. (1979), Grindlay et al. (1980), and Halpern (1982). The counts were collected in eight pulse height analyzer (PHA) bins placed at approximately logarithmic energy intervals over the 1–20 keV bandpass. The energy resolution was approximately 20% at 6 keV. The width of the MPC energy channels were adjusted to get agreement with the previously determined photon index and normalization (Torr & Seward 1972) using

© American Astronomical Society • Provided by the NASA Astrophysics Data System

1991ApJS...76.1127V

TABLE 1

LOG OF OBSERVATIONS

Source[a]	Sequence Number	Grating	UT Time of Observation[b] Start Year	Start Day	Start Second	Stop Year	Stop Day	Stop Second	Net Time on Source (s) OGS	Net Time on Source (s) MPC
I. Massive Systems (HMXBs)[c]										
4U1516-56 Cir X-1	6624	1000	1980	48	46051.2	1980	48	72000.9	5000.0	3071.9
4U1700-37 (V884 Sco)	6622	1000	1980	75	15430.1	1980	75	23130.6	5400.0	4218.0
4U1956+35 Cyg X-1 (HDE226868)	820	1000	1979	136	5559.3	1979	137	23279.7	13625.0	8683.3
II. Intermediate mass										
4U1656+35	3364	500	1979	75	53481.6	1979	76	62718.9	45960.0	32320.0
Her X-1	High[d]								6248.0	3124.0
(HZ Her)	Spike[d]								2089.0	2089.0
	Low[d]								12509.0	12509.0
	631	1000	1979	74	4345.6	1979	74	65616.9	10895.0	5939.0
	632	500	1979	75	19785.6	1979	75	41926.6	7830.0	4915.0
	633	500	1979	75	42076.8	1979	75	53313.5	6561.9	
III. Low-mass Systems (LMXBs)										
4U1617-15	826	1000	1981	33	46051.2	1981	33	57283.2	4858.2	...[e]
Sco X-1	9537	1000	1981	33	57456.0	1981	33	66873.6	4627.8	...
(V818 Sco)	9538	1000	1981	46	44496.0	1981	46	51667.2	4396.2	...
	8338	1000	1981	79	24019.2	1981	79	44668.8	7487.4	...
4U1626-67 (KZ TrA)	2845	1000	1979	73	669.7	1979	73	18733.0	9287.0	11919.3
4U1636-53	2844	1000	1979	73	50067.4	1979	73	65345.5	9728.0	4464.4
(V801 Ara)	710	500	1979	74	66108.4	1979	75	6701.0	14158.0	13598.4
	6769	1000	1980	75	46232.0	1980	75	55448.0	6416.0	3276.7
4U1659-48 GX339-4 (V821 Ara)	6623	1000	1980	76	9762.3	1980	76	20657.6	6900.0	4054.8
4U1728-16	6762	1000	1980	88	10315.2	1980	88	25101.8	7641.0	286.6
GX9+9	10367	1000	1981	77	79041.6	1981	78	15087.3	12409.6	9912.3
(V2216 Oph)										
4U1735-44 (V926 Sco)	6764	1000	1980	75	55734.7	1980	75	68145.6	6743.0	6102.9
4U1813-14 GX17+2	6767	1000	1980	88	83674.6	1980	89	2763.2	3173.0	1597.4
4U1837+04	6768	1000	1980	88	59713.0	1980	88	75974.1	7491.4	6184.7
Ser X-1	10649	1000	1981	95	67296.4	1981	96	6414.5	13187.5	9338.9
(MM Ser)										
4U2142+38	824	1000	1979	136	28292.1	1979	136	64500.8	15158.0	12861.0
Cyg X-2	824HI[f]								8192.0	8192.0
(V1341 Cyg)	824DP[f]								2007.0	2007.0
	824ND[f]								2662.4	2662.4

© American Astronomical Society • Provided by the NASA Astrophysics Data System

1991ApJS...76.1127V

TABLE 1—*Continued*

Source[a]	Sequence Number	Grating	UT Time of Observation[b] Start Year	Start Day	Start Second	Stop Year	Stop Day	Stop Second	Net Time on Source (s) OGS	MPC
IV. Globular Cluster Sources										
4U1728-33 GX354-0	6763	1000	1980	88	812.5	1980	88	30631.4	8647.0	3317.7
4U1820-30	708A[g]	1000	1979	73	35403.7	1979	73	49616.9	9759.2	7185.9
in NGC 6624	708B	1000	1979	74	27319.3	1979	74	35511.3	4556.4	4894.7
V. Optically Unidentified Sources										
4U1642-45 GX340+0	6761	1000	1980	75	84160.0	1980	76	9393.6	7714.0	6512.5
4U1702-36 GX349+2	822	1000	1979	73	81524.7	1979	74	18267.0	4577.0	8765.3
4U1744-26 GX3+1	6765	1000	1980	88	30877.2	1980	88	43861.5	4013.0	2129.9
4U1758-20 GX9+1	6770	1000	1980	88	76342.8	1980	88	83510.8	4783.0	2088.9
4U1758-25 GX5-1	2843	1000	1979	74	35879.9	1979	74	42965.0	3916.0	2990.0
4U1811-17 GX13+1	6766	1000	1980	88	46073.3	1980	88	59385.3	6707.0	5652.3

[a] Names in parentheses refer to optical counterparts.
[b] Start and stop times for pointings are the same in both detectors since the MPC was co-aligned with the focal-plane instrument, in this case the OGS.
[c] Classifications from Bradt & McClintock 1983.
[d] Subsets within observations according to spectral state as mentioned in Vrtilek & Halpern 1985.
[e] MPC observations not usable due to counter overflow.
[f] Subsets within observations according to spectral state as mentioned in Vrtilek et al. 1986b.
[g] Subsets within observations according to spectral state as mentioned in Vrtilek et al. 1986a.

an average of 30 in-flight observations of the Crab taken with the MPC (Arnaud 1990). Arnaud also modified the MPC data extraction and background subtraction from the method described in Halpern (1982) in several ways: (1) McIlwain *l* and *B* parameters were used to eliminate data with *l* greater than 1.2 and *B* less than 0.25 (effectively removing data contaminated by the South Atlantic Anomaly); (2) The contribution to the background caused by the decay of the in-flight calibration source (^{109}Cd) was modeled and found to give a good fit to an exponential with a half-life of 450.4 days; (3) The model to predict the background used the pulse shape (PSDI) and rise time (PSDT) discriminator rates which were found to have good correlations with the background rates, after correcting for the half-life of the ^{109}Cd. Halpern had noted the need for correcting for the ^{109}Cd decay but had been unable to do so because time-ordered processing of the data, since completed, was required. The MPC effective area used in this study is shown in Figure 3.

3. DATA REDUCTION AND RESULTS

3.1. *Joint Analysis of* OGS *and* MPC

Since the OGS was limited to a narrow energy range, the models for the source continua were fitted to the MPC and OGS data simultaneously. The good response at high energies and the broad spectral coverage of the MPC allowed us to constrain continuum temperatures, whereas the response at low energies and high spectral resolution of the OGS was ideal for measuring column densities. A schematic of the joint MPC and OGS analysis procedure is shown in Figure 4. The methods of extracting the dispersed spectra and background are described in detail by KSC84. The profile of the zero order was used as the point response function. In this study, the two first-order spectra of the OGS were combined by folding across the center of the zero order (except in the case of Sco X-1, for which the image was positioned at the edge of the HRI so that only one first-order spectrum was detected.) The OGS data

© American Astronomical Society • Provided by the NASA Astrophysics Data System

1991ApJS...76.1127V

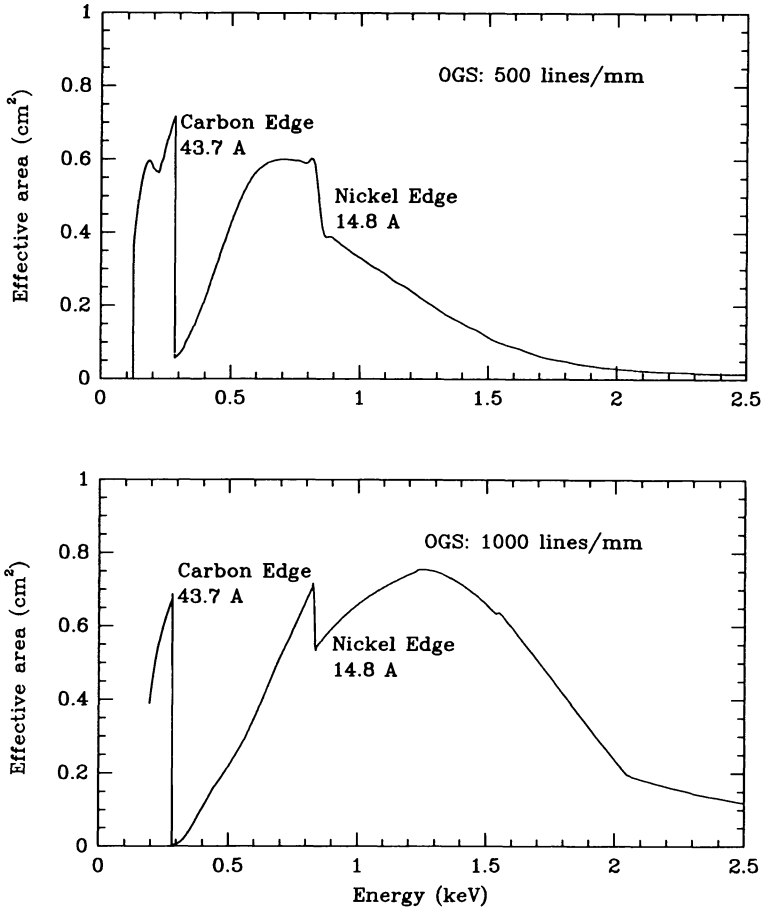

FIG. 2.—OGS effective areas vs. photon energy. *Upper panel:* 500 lines mm^{-1} grating. *Lower panel:* 1000 lines mm^{-1} grating. The neutral carbon edge in the 1000 lines mm^{-1} grating is deeper than that in the 500 lines mm^{-1} due to a parylene coating applied for structural support on the finer grating. The nickel edge is from the mirror coating.

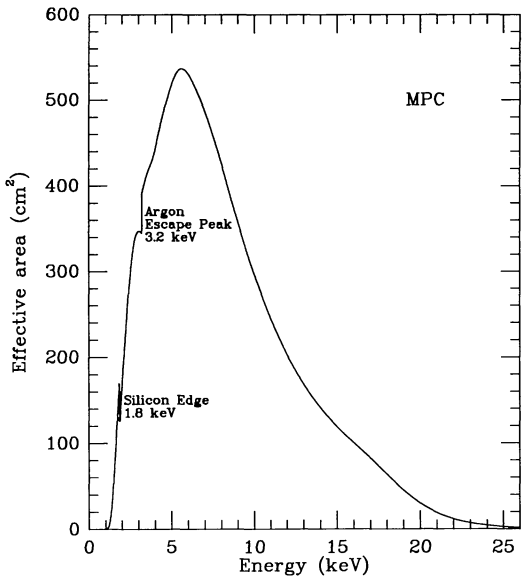

FIG. 3.—MPC effective area vs. energy. The argon K-escape peak at 3.2 keV is caused by the gas in the proportional counters.

were sorted into bins of width 0.3 Å, a wavelength band slightly narrower than the instrument resolution.

As a test of the combined MPC and OGS processing, a least-squares fit was performed to an observation of the Crab Nebula taken simultaneously with the OGS and the MPC. With the power-law index, interstellar absorption, and normalization as free parameters and using the interstellar absorption coefficients of Morrison & McCammon (1983, hereafter MM83), the best-fit parameters (illustrated in Fig. 5) are photon index $\alpha = -2.17 \pm 0.04$, $N_H = 3.47 \pm 0.05 \times 10^{21}$ cm^{-2}, and normalization of 10.47 ± 0.5 (cm^{-2} s^{-1} keV^{-1}). The difference in measured equivalent hydrogen column density from the value used to calibrate the OGS ($N_H = 3.1 \pm 0.2 \times 10^{21}$ cm^{-2} from Charles et al. 1979) is due to the fact that MM83 used a higher oxygen abundance than that of Brown & Gould (1970). Using the MM value $[(O/H)_{MM} = 7.41 \times 10^{-4}]$ the neutral column density of oxygen is constrained by the data to be $2.8 \pm 0.2 \times 10^{18}$ cm^{-2}, a value in excellent agreement with that from Charles et al. ($2.7 \pm 0.2 \times 10^{18}$ cm^{-2}). The excellence of the fit is not surprising since the final calibrations of the MPC and the OGS, although done independently, both utilized in-flight observations of the Crab. Since

© American Astronomical Society • Provided by the NASA Astrophysics Data System

1991ApJS...76.1127V

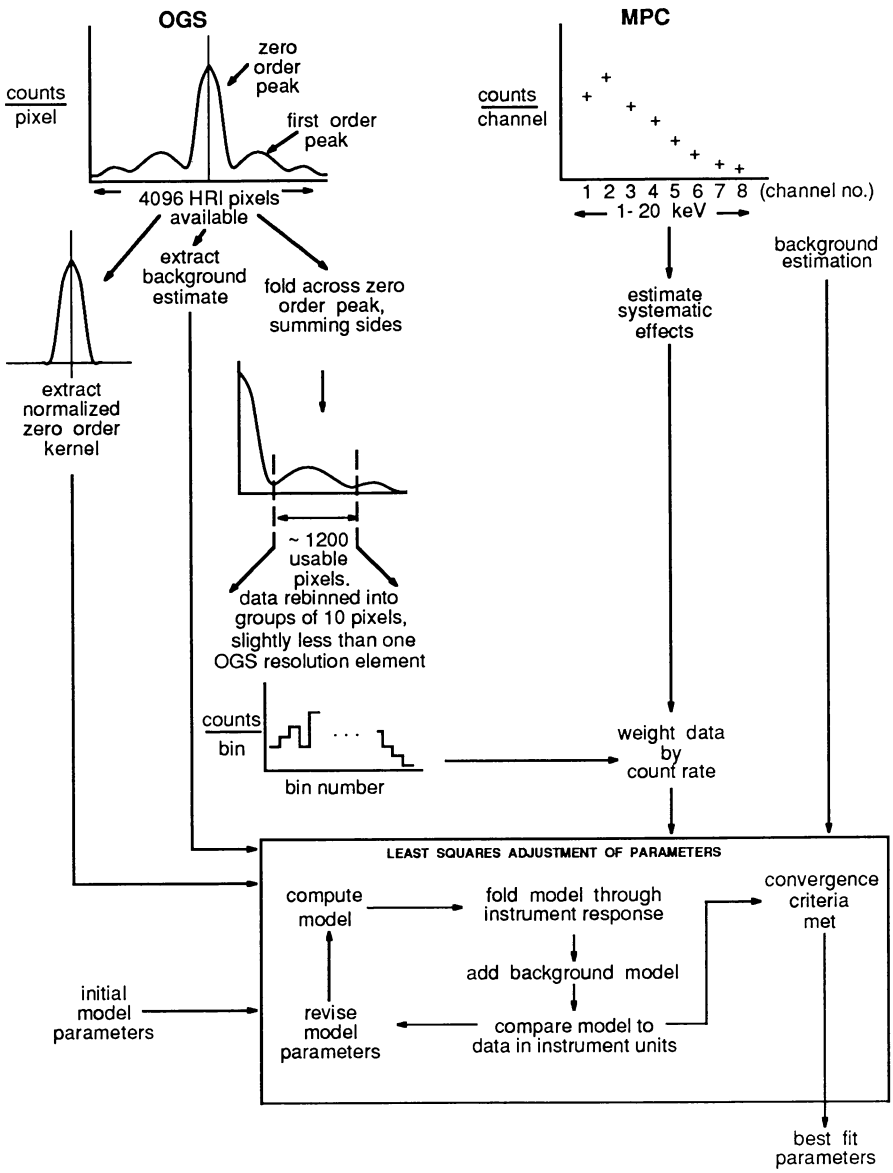

FIG. 4.—Schematic of *Einstein* Objective Grating Spectrometer and Monitor Proportional Counter joint data analysis

the spatial extent of the Crab Nebula is 1′, equivalent to 3.7 Å (10 times the resolution of the OGS) in the first-order spectrum of the 1000 lines mm^{-1} grating, the sharp Ni edge at 14.5 Å has been broadened and does not appear in the raw count spectrum of Figure 5, although it is clearly visible in the spectra of some point sources (e.g., Figs. 15 and 17). The Ni edge does not appear in the model, either, because that has been convolved with the zero-order peak, also broadened here by the spatial extent of the Crab.

3.2. *Signal-to-Noise Ratios*

The MPC had a peak effective area of 540 cm^2 at ~5 keV (Fig. 3), giving high signal-to-noise ratios; however, it had poor spectral resolution with considerable overlap in energy among the eight channels. The OGS, on the other hand, had relatively high spectral resolution, but with an effective area of <1 cm^2 (Fig. 2) it yielded modest signal-to-noise ratio for even strong sources. The signal-to-noise ratio is defined as

$$\mathrm{S/N} = \frac{C_{T-B}}{\sigma_C} \qquad (1)$$

where C_{T-B} = (total counts − background model counts), and σ_C is given by (total counts + $\sigma^2_{\mathrm{systematic}} + \sigma^2_{\mathrm{background}})^{1/2}$ for the MPC and (total counts)$^{1/2}$ for the OGS. Values of S/N are listed for each source at several energies for both instruments in Table 2. For the MPC, S/N was computed for the channel that includes the quoted energy; for the OGS, S/N was computed per resolution element, using as the total count value the mean of six resolution elements centered on the quoted energy. We note that the S/N ratios given for the OGS are somewhat overestimated since we take into account only statistical

© American Astronomical Society • Provided by the NASA Astrophysics Data System

1991ApJS...76.1127V

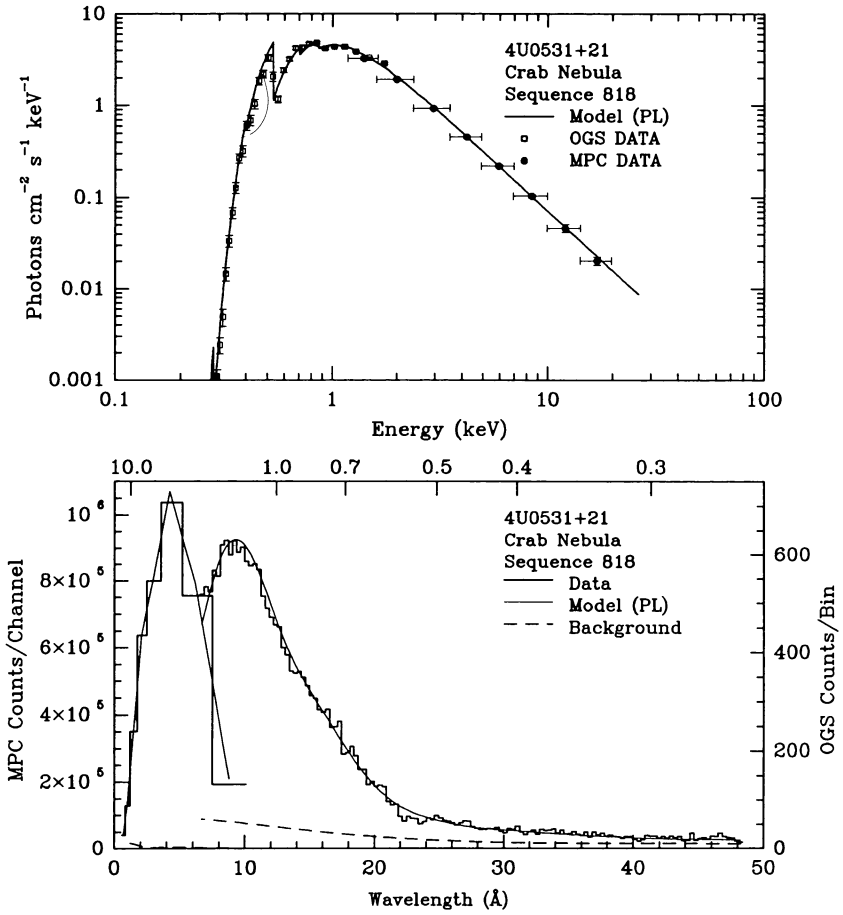

FIG. 5.—*Upper panel:* Photon spectrum for the Crab Nebula using MPC and OGS data combined. Each OGS point shown represents four resolution elements (1.6 Å); the bars indicate 1 σ errors. Channel boundaries and 1 σ errors are indicated for the MPC channels by the widths and heights of the crosses, respectively. The model is a power law (PL) with adjustable absorption (§ 3.1). *Lower panel:* MPC and OGS raw count spectrum of the Crab Nebula. MPC counts per channel are designated on the left ordinate, OGS counts per 0.3 Å bin for the 1000 lines mm^{-1} grating are designated on the right ordinate. The ordinate scales are adjusted to the full range for each instrument. The lower abscissa designates wavelength in angstroms, and the upper abscissa designates energy in keV. Counts are plotted as solid histograms, the measured background as dashed lines, and the best-fit models as solid curves.

errors. The greatest source of background for the OGS was due to low-level, large angle scattering of the zero-order photons, associated with imperfections on the mirror surface (S82). Up to 70% of the zero-order flux at energies greater than 1 keV is distributed in broad wings prominent out to approximately 18 Å along the dispersion direction. In the majority of cases, this scattering is circularly symmetric, and background was measured by examining the intensity of the scattering wings as a function of radius perpendicular to the dispersion direction. The derived background is accurate to about 10% (KSC84). For the brightest sources, this makes background uncertainties negligible in relation to errors from counting statistics. Another source of error for the gratings is the contribution of higher orders to the first-order fluxes. The contributions of the higher orders were evaluated using theoretical predictions of the ratios of each order to the zero order, which were found to be in excellent agreement with the data for the 1000 lines mm^{-1} grating and consistently higher than measured for the 500 lines mm^{-1} grating (S82).

3.3. *Continuum Fits*

We performed least-squares fits to the data of simple, single-component models for the continuum photon spectra; the models are of the form:

$$N(E)(\mathrm{cm}^{-2}\,\mathrm{s}^{-1}\,\mathrm{keV}^{-1}) = (\mathrm{MODEL}) * e^{-N_{\mathrm{H}}\sigma(E)}\,, \quad (2)$$

where $\sigma(E)$ is the photoelectric absorption cross section obtained by considering the effect of all the heavy elements at their cosmic abundances as defined by MM83, and N_{H} is the total neutral hydrogen column density. Here MODEL can stand for either a blackbody, a power-law, or an optically thin thermal bremsstrahlung spectrum with photon fluxes, respectively, of the form:

$$A_{\mathrm{BB}}(e^{E/kT} - 1)^{-1}(E/E_0)^2\,, \quad (3)$$

$$A_{\mathrm{PL}}(E/E_0)^{-\alpha}\,, \quad (4)$$

© American Astronomical Society • Provided by the NASA Astrophysics Data System

1991ApJS...76.1127V

$$A_{\rm TB} e^{-E/kT} (E/E_0)^{-1} g(E; kT) , \quad (5)$$

where $A_{\rm BB}$, $A_{\rm PL}$, and $A_{\rm TB}$ are the normalization constants (cm^2 s^{-1} keV^{-1}), E is the photon energy in keV, (E/E_0) is the photon energy normalized to 1 keV, T is the temperature in kelvins, k is the Boltzmann constant, α is a power-law index, and $g(E; kT)$ is the Gaunt factor (Kellogg, Baldwin, & Koch 1975). For Her X-1, we made an exception to the use of single-component models and employed a well-known two-component model consisting of a power-law plus blackbody (McCray et al. 1982). We modified the nonlinear least-squares model-fitting program used by KSC84 for their OGS analysis to provide a variance-covariance matrix of the model parameters that can be used to determine the correlation between the parameters. This technique shows high correlations between temperature, normalization, and column density when either the OGS or the MPC data are used alone. Fits to the MPC data alone fall below the data from the low-energy OGS channels, due to an overestimate of the column density; fits to the OGS data alone fall below the data from the high-energy MPC because they underestimate the temperature. We find that fitting the MPC and OGS data together greatly reduces these correlations (from $\geq$0.99 to $\leq$0.90), resulting typically in reductions of uncertainty in temperature and column density by factors of 3–5, hence in a more reliable determination of the model parameters (Vrtilek et al. 1986b, hereafter Vrt86b). The joint MPC and OGS fit is thus very important for reliable determination of spectral parameters.

The best-fit parameter values for each source are listed in Table 3 along with the 2–10 keV flux as observed by the MPC. The massive systems favored (in the sense of minimum χ_ν^2) power-law (PL) models and the low-mass systems thermal models (either bremsstrahlung [TB] or blackbody [BB]). For the nine sources with TB spectra the continuum emission measures ranged from 2.6×10^{58} to 1.5×10^{61} cm^{-3}, where the emission measure, under the assumption of a uniform emitting region, is given by

$$n_e n_i V (\rm cm^{-3}) = 3.51 \times 10^{58} A_{\rm TB} [D(\rm kpc)]^2 [kT(\rm keV)]^{1/2} , \quad (6)$$

where D is the distance to the source (when the distance is not known, 8 kpc was assumed). The effective radii of the emitting material, calculated for the eight sources which favored a BB spectrum, and given by

$$R(\rm km) = 3.11 D(\rm kpc) (A_{\rm BB})^{1/2} , \quad (7)$$

ranged from 6 to 10 km, roughly consistent with the expected size of a neutron star. The soft blackbody component of one exceptional source, Her X-1, implies a much larger emitting region (ranging from 170 to 320 km), which has been interpreted as due to reprocessing of the central X-rays at the magnetospheric boundary (McCray et al. 1982). It should be noted that Her X-1 is considerably above the Galactic plane (b = 37.5), and the higher column densities observed for most sources may have prevented detection of similar soft components.

3.4. *Column Densities*

The X-ray column densities derived from the combined MPC and OGS fits range from 4.0×10^{19} to 5.0×10^{23} cm^{-2}. The values of $N_{\rm H}$ obtained are weakly correlated with the spectral temperatures obtained from model fitting (with typical correlation coefficients from -0.7 to -0.9). We note that the values of $N_{\rm H}$ derived here are actually lower limits to the true column densities, because of the possible presence of ionized material. The lowest measured neutral hydrogen column densities in any direction reported for the ISM in our Galaxy is 4.5×10^{19} cm^{-2} derived from 21 cm observations (Lockman, Jahoda, & McCammon 1986). The lowest value of column density we obtained ($4.0 \pm 0.5 \times 10^{19}$ cm^{-2}) is comparable to this value. The source that displayed this value (Her X-1) also gave (during a different binary phase) the highest value of column density (5.0×10^{23} cm^{-2})!

The measured $N_{\rm H}$ values were converted to equivalent visual extinction by the empirical formula:

$$A_v^{\rm X\text{-}ray} = \frac{3(N_{\rm H} - 2.14 \times 10^{20})}{3.91 \times 10^{21}} \quad (8)$$

taken from Heiles, Stark, & Kulkarni (1981). The superscript $^{\rm X\text{-}ray}$ is used to distinguish the X-ray determined values from optically determined $A_v^{\rm opt}$. The computed values of $A_v^{\rm X\text{-}ray}$ and the optical extinction $A_v^{\rm opt}$ as has been determined or estimated for 15 sources (BMC83) are listed in Table 4. The extinction $A_v^{\rm X\text{-}ray}$ implied by measured $N_{\rm H}$ is always greater than or approximately equal to optically measured $A_v^{\rm opt}$ (Fig. 6a). Where multiple observations of a source exist, considerable variability can be observed in $N_{\rm H}$ around the binary orbit, the most striking example being Her X-1, as noted above. Both the higher values of $A_v^{\rm X\text{-}ray}$ and the variability of $N_{\rm H}$ implies that many of the X-ray binaries studied have components of column density intrinsic to the sources, in agreement with the result of Gorenstein (1975). The "intrinsic" column density as measured by $A_v^{\rm X\text{-}ray} - A_v^{\rm opt}$ is plotted versus $A_v^{\rm opt}$ in Figure 6b.

Fitting a cosecant law to the lowest measured $A_v^{\rm X\text{-}ray}$ for each source using

$$A_v = \zeta \cdot \csc |b| , \quad (9)$$

where b is the Galactic latitude, gives a ζ of 0.08 ± 0.06 for $A_v^{\rm opt}$ and 0.34 ± 0.06 for $A_v^{\rm X\text{-}ray}$ (Fig. 7a). Not surprisingly, the extinction is very high toward the Galactic plane. The correlation of $A_v^{\rm X\text{-}ray}$ with Galactic latitude is better demonstrated when the cosecant dependence of latitude is eliminated (Fig. 7b). The systems show a weak correlation of $A_v^{\rm X\text{-}ray}$ with Galactic latitude (correlation coefficient $r = 0.62 \pm 0.1$).

3.5. *Abundance Anomalies*

All observations for which χ_ν^2 values for the continuum fits were greater than 1.5 were checked for anomalous abundances of C, N, and O relative to the "cosmic" values given by MM83. The OGS is well able to detect the neutral absorption edges of these elements (at 43.68, 30.99, and 23.32 Å, respectively) with high statistical significance in the brightest sources. However, the presence of an instrumental carbon edge makes car-

© American Astronomical Society • Provided by the NASA Astrophysics Data System

1991ApJS...76.1127V

TABLE 2

TYPICAL SIGNAL-TO-NOISE RATIOS AT VARIOUS ENERGIES[a]

Source[b]	OGS			MPC		
	0.3 keV (0.29-0.31)	0.6 keV (0.57-0.64)	1.0 keV (0.90-1.10)	3.0 keV (2.42-3.56)	6.0 keV (4.98-7.05)	12 keV (10.10-14.37)
I. Massive Systems (HMXBs)						
4U1516-56 Cir X-1	<1	< 1	< 1	39	15	2
4U1700-37	< 1	1	< 1	201	336	155
4U1956+35 Cyg X-1	1	4	13	778	772	344
II. Intermediate-mass System						
4U1656+35 Her X-1 (631)	3	5	3	331	388	201
III. Low-mass Systems (LMXBs)						
4U1617-15 Sco X-1 (8338)	3	4	5	...	...	...
4U1626-67	< 1	1	3	245	185	67
4U1636-53 (710)	1	5	10	613	447	93
4U1659-48 Sco X-2	1	3	10	720	213	< 1
4U1705-4	< 1	< 1	1	602	648	195
4U1728-16 GX9+9 (10367)	1	3	8	646	979	476
4U1735-44	2	4	1	575	526	157
4U1813-14 Gx17+2	1	2	6	488	529	160
4U1837+04 Ser X-1 (10649)	1	2	6	567	480	140
4U2142+38 Cyg X-2 (824hi)	1	4	11	730	550	110
IV. Globular Cluster Sources						
4U1728-33 GX354-0	< 1	< 1	< 1	205	259	88
4U1820-30 (708A)	1	5	11	800	770	250
V. Optically Unidentified Sources						
4U1642-45 GX340+0	< 1	< 1	< 1	630	919	303
4U1702-3 GX349+2	<1	1	5	127	1361	427
4U1744-26 GX3+1	<1	< 1	1	328	312	69

© American Astronomical Society • Provided by the NASA Astrophysics Data System

1991ApJS...76.1127V

TABLE 2—*Continued*

Source	OGS			MPC		
	0.3 keV (0.29-0.31)	0.6 keV (0.57-0.64)	1.0 keV (0.90-1.10)	3.0 keV (2.42-3.56)	6.0 keV (4.98-7.05)	12 keV (10.10-14.37)
4U1758-20 GX9+1	< 1	< 1	1	460	479	133
4U1758-25 GX5-1	<1	1	1	871	1008	293
4U1811-17 GX13+1	< 1	< 1	1	646	677	174

[a] The signal-to-noise ratio, given for one resolution element in the OGS and for the channel encompassing the given energy in the MPC, is defined in the text.

[b] Where multiple observations exist, the observation with the highest flux in the 2–10 keV range was used, and the corresponding sequence number is given in parentheses.

bon abundance determinations suspect. The fitted abundances and spectral parameters for the cases which resulted in a significant reduction in χ^2 are given in Table 5, where the abundances are given as

$$[X/H] = \log (X/H) - \log (X/H)_{MM} , \qquad (10)$$

where X/H is the abundance of element X in the absorbing medium and $(X/H)_{MM}$ is the abundance of element X as given by MM83. $(O/H)_{MM} = 7.41 \times 10^{-4}$, $(N/H)_{MM} = 0.91 \times 10^{-4}$, and $(C/H)_{MM} = 4.47 \times 10^{-4}$, and the log abundance of H is assumed to be 12. The algorithms for computing oxygen, carbon, and nitrogen absorption cross sections were provided by D. McCammon (1987, personal communication). Figures 8 and 9 demonstrate the improvement to the fit when the measured anomalous abundances are applied for Sco X-1 and Cyg X-1; both these sources require a significant increase from the cosmic in the abundance of nitrogen. The abundance anomalies detected in these sources is suggestive of CNO processing associated with hydrogen burning.

3.6. *Emission Lines*

Soft X-ray emission lines attributable mainly to N, O, Fe, and Si appear in the spectra of 11 of the sources studied at a formal detection level greater than 3 σ. The line features with their associated equivalent widths are listed in Table 6. For four sources in addition to those listed in Table 6 we detected excess emission between 8 and 40 Å (4U 1656+35; 4U 1659−48; 4U 1702−36; and 4U 1758−25) but without sufficient statistics to identify individual line features. Some of these observations have already been discussed in the literature (KSC84; Vrt86a; Vrt86b; Freeman, Kahn, & Vrtilek 1991; KVK89; Liedahl et al. 1990). Since the emission and absorption features are weak and superposed on a strong, highly sloping continuum, it is necessary to subtract the continuum from the raw count spectra in order to isolate features. It is important to note that even a very slight change in continuum slope can affect the strengths of the features and in extreme cases can even change emission features to absorption features, so our results are very much dependent on the accuracy of the continuum fits.

The tentative line "identifications" were made using the tables of Kato (1976), Raymond & Smith (1977), Doschek & Cowan (1984), and Wiese (1985). In some cases, such as that of the strong features attributed to Fe XVII, the features are sufficiently distinct that the identification is almost certainly correct. However, many of the features can only be associated with line complexes due to the high density of possible emission lines in the vicinity. (Specific line features observed in the strongest sources [Cyg X-1, Sco X-1, and Cyg X-2] have been confirmed by *EXOSAT* TGS observations [Freeman et al. 1991; Chiappetti et al. 1990; Brinkman et al. 1985].)

A possible site for the soft X-ray line-emission from LMXBs is an X-ray–illuminated corona above the accretion disk. The extended X-ray eclipses independent of energy that have been found in several LMXBs provide empirical evidence for the presence of accretion disk coronae (ADC) (McClintock et al. 1982; Mason 1986 and references therein). The emission measure for a corona optically thin to Thompson scattering is given by KVK89 as

$$EM = 3.6 \times 10^{61} \frac{L_{38}^2 f^2}{T_7^{3/2} R_9^{1/2}} , \qquad (11)$$

where EM is in cm^{-3}, L_{38} is the source luminosity in units of 10^{38} ergs s^{-1}, f is a factor that corrects for angle of incidence, T_7 is the coronal temperature in units of 10^7 K, and R_9 is the distance from the source to the emitting region in units of 10^9 cm. The emission measures range from 10^{56}–10^{58} cm^3. Some of the spectral features observed can be roughly reproduced as emission from such an optically thin collision-dominated gas, but there are significant discrepancies between observed and predicted strengths and shapes of the strong features (KVK89; Kallman et al. 1991). The features are not consistent with an isothermal emission region, but rather require a range of temperature from 10^6 to 10^8 K, with the short-wavelength (below 20 Å) features preferentially emitted by higher temperature material.

© American Astronomical Society • Provided by the NASA Astrophysics Data System

1991ApJS...76.1127V

TABLE 3

SPECTRAL PARAMETERS FOR SIMPLE CONTINUUM FITS

Source	Model type[a] and sequence	A (cm^{-2} s^{-1} keV^{-1})	kT or α[b]	log N_H (cm^{-2})	χ^2_ν and dof[c]	2-10 keV flux (erg $cm^{-2}s^{-1}$)
I. Massive (HMXBs)						
4U1516-56 Cir X-1	PL(6624)	0.30±0.10	3.47±0.8	22.60±0.50	1.2(5)	0.1 × 10^{-9}
4U1700-37	PL(6622)	0.38±0.08	1.33±0.09	22.84±0.05	1.6(141)	2.3 × 10^{-9}
4U1956+35 Cyg X-1	PL(820)	1.55±0.03	1.75±0.04	21.57±0.03	3.1(155)	7.9 × 10^{-9}
II. Intermediate mass						
4U1656+35 Her X-1	PL + BB(3364)	0.13±0.40 417.00± 0.15	0.93±0.17 0.12±0.02	19.93±2.2[d] 23.11±1.0[e] 23.70±0.8[f]	1.1(83)	2.5 × 10^{-9}
	PL + BB(631)	0.10±1.31 124.45±3.91	0.72±1.46 0.13±0.31	19.60±0.80	1.28(76)	2.8 × 10^{-9}
	PL + BB(632)	0.12±0.42 134.90±0.69	0.84±0.52 0.13±0.05	19.60±2.58	1.24(76)	2.6 × 10^{-9}
	BB(633) OGS only	245.47±0.05	0.12±0.01	19.97±0.05	0.9(132)	...
III. Low-mass (LMXBs)						
4U1617-15 Sco X-1	TB(826)	28.1±0.17	2.98±0.75	21.34±0.10	3.4(174)	...
	TB(9537)	128.8±0.37	1.07±0.52	21.61±0.13	2.5(170)	...
	TB(9538)	82.8±0.28	1.40±0.63	21.59±0.09	2.4(170)	...
	TB(8338)	26.1±0.38	3.33±4.14	21.45±0.12	3.7(170)	...
4U1626-67	PL(2845)	0.12±0.03	1.68±0.05	21.39±0.07	1.0(141)	0.7 × 10^{-9}
4U1636-53	PL(710)	0.93±0.03	2.25±0.03	21.62±0.03	1.9(139)	2.6 × 10^{-9}
	PL(2844)	0.38±0.03	1.98±0.04	21.75±0.04	1.7(139)	1.9 × 10^{-9}
	PL(6769)	0.67±0.04	2.27±0.05	21.84±0.05	2.4(137)	1.7 × 10^{-9}
4U1659-48 GX339-4	TB(6623)	13.74±0.02	1.28±0.02	21.82±0.02	1.5(137)	8.0 × 10^{-9}
4U1705-44	BB(6621)	0.10±0.05	2.45±0.50	22.09±0.30	1.2(139)	10.6 × 10^{-9}
4U1728−16	TB(6762)	0.93±0.06	7.40±0.40	21.50±0.12	1.5(136)	8.7 × 10^{-9}
GX9+9	TB(10367)	0.95±0.05	7.65±0.25	21.59±0.09	1.6(136)	9.6 × 10^{-9}
4U1735-44	TB(6764)	0.43±0.03	11.14±0.7	21.71±0.03	1.8(137)	5.6 × 10^{-9}
4U1813-14 GX17+2	BB(6767)	0.31±0.04	1.51±0.03	22.17±0.04	1.9(139)	17.0 × 10^{-9}
4U1837+04	TB(6768)	0.82±0.02	5.9±0.20	21.92±0.13	0.6(139)	5.8 × 10^{-9}
Ser X-1	TB(10649)	0.91±0.02	6.9±0.22	21.84±0.12	1.1(139)	7.8 × 10^{-9}
4U2142+38	TB(824hi)	2.29±0.01	5.61±0.10	21.57±0.02	1.5(148)	17.2 × 10^{-9}
Cyg X-2	TB(824dp)	1.71±0.02	5.25±0.15	21.52±0.02	1.6(148)	12.0 × 10^{-9}
	TB(824nd)	2.70±0.02	4.71±0.21	21.48±0.02	1.4(148)	18.0 × 10^{-9}
IV. Globular Clusters Sources						
4U1728-33 GX354-0	BB(6763)	0.02±0.05	1.78±0.05	22.17±0.07	0.9(145)	2.1 × 10^{-9}
4U1820-30	TB(708A)	0.78±0.03	12.69±0.91	21.28±0.03	1.1(131)	11.4 × 10^{-9}
	TB(708B)	0.84±0.02	9.85±0.50	21.30±0.03	1.1(131)	10.2 × 10^{-9}

© American Astronomical Society • Provided by the NASA Astrophysics Data System

1991ApJS...76.1127V

TABLE 3—*Continued*

Source	Model type[a] and sequence	A (cm^{-2} s^{-1} keV^{-1})	kT or α[b]	log N_H (cm^{-2})	χ^2_ν and dof[c]	2-10 keV flux (erg $cm^{-2}s^{-1}$)
V. Optically Unidentified Sources						
4U1642-45 GX340+0	BB(6761)	0.12±0.04	1.77±0.04	22.59±0.04	1.1(139)	10.3×10^{-9}
4U1702-36 GX349+2	BB(822)	0.31±0.03	1.57±0.03	21.69±0.05	1.9(149)	20.8×10^{-9}
4U1744-26 GX3+1	TB(6765)	0.97±0.03	5.83±0.24	22.46±0.02	0.9(139)	5.2×10^{-9}
4U1758-20 GX9+1	TB(6770)	1.49±0.05	8.68±0.84	22.49±0.03	0.6(139)	11.2×10^{-9}
4U1758-25 GX5-1	BB(2843)	0.60±0.04	1.48±0.03	22.30±0.04	0.8(145)	30.3×10^{-9}
4U1811−17 GX13+1	BB(6766)	0.19±0.05	1.41±0.04	22.26±0.05	0.9(139)	8.2×10^{-9}

[a] PL, TB, and BB stand for power-law, thermal bremsstrahlung, and blackbody.
[b] kT (keV) applies to TB and BB models, α to PL.
[c] Numbers in parentheses are the degrees of freedom used to compute values of χ^2_ν.
[d] Subset of sequence 3364: high state of 35 day cycle as defined in Vrtilek & Halpern 1985.
[e] Subset of sequence 3364: spike state of pre-eclipse dip as defined in Vrtilek & Halpern 1985.
[f] Subset of sequence 3364: nonspike state of pre-eclipse dip as defined in Vrtilek & Halpern 1985.

It is quite likely that many of these features originate in photoionized gas, in which case significant departures from standard collisional line spectra are expected (Liedahl et al. 1990). Liedahl et al. 1990 compare these two well-defined processes; for the photoionized case, they use the ionization and energy balance equations of Kallman & McCray (1982) (but increase the detail in atomic models for Fe XVI–XIX in order to facilitate spectral modeling). For the collisional case they use calculations for the same ions, under conditions appropriate to coronal equilibrium. While Liedahl et al. neglect contributions from higher ionization states of Fe and from other elements, they are able to show definitively that significant differences exist in lines formed by these two processes. The Fe features they predict using both photoionized and collisional processes are detected in the OGS observations, often coexisting in the same observation.

The fitting procedures used by Vrt86a, KVK89, and Kallman et al. (1991) assumed that the lines are attenuated by the same optical depth of photoelectric absorption as the continuum. The lack of a correlation between line equivalent widths and N_H is consistent with this assumption. In Figure 10 we plot the equivalent widths of selected lines (those at 9.0 Å and 11.6 Å attributed to Fe XXII, at 15.3 Å attributed to Fe XVII, and at 16.0 Å and 19.0 Å attributed to O VIII) versus N_H for all sources in which they are observed. Photoelectric absorption is likely to be dominated by material which is much cooler and less ionized than that responsible for the line emission. Since such cool material is expected to occur only at large distances from the X-ray source, the emission lines and continuum are both likely to traverse equal column densities and undergo the same attenuation.

In Figure 11 are plotted the measured X-ray column densities versus the 2–10 keV flux. It is clear that sources which were barely detected in the OGS combined high column density with low flux (*stars*), sources that showed significant line emission combined low column density with high flux (*filled circles* and *filled squares*).

3.7. *Absorption Edges*

Since the high resolution of the OGS allowed us to detect the absorption edges due to a few individual elements (O, Fe, Ne), we were able in some cases to obtain measures of column density independent of the abundances assumed in the MM83 absorption model. This is true in particular for the K absorption edge of oxygen at 0.532 keV, which is sufficiently strong for us to attempt individual measurement in several sources. In Table 7 we list the optical depths τ where

$$e^{-\tau} = \frac{I_{\rm abs}}{I_{\rm cont}}, \qquad (12)$$

where $I_{\rm abs}$ is the absorbed flux at the edge (computed for three resolution elements in the OGS) and $I_{\rm cont}$ is the fitted continuum flux. The O K-edge at $\approx$0.5 keV is detected in 10 sources; the Fe L-edge at $\approx$0.7 keV and the Ne K-edge at $\approx$0.9 keV are detected in seven sources. We note that those sources studied with the Solid State Spectrometer (SSS) on the *Einstein Obser-*

© American Astronomical Society • Provided by the NASA Astrophysics Data System

1991ApJS...76.1127V

TABLE 4

MEASURED EXTINCTION

Source (Seq. No.)	log N_H (cm^{-2})	D[a] (kpc)	A_v^{opt}	A_v^{x-ray}	Galactic latitude b^{II}(degrees)
I. Massive Systems (HMXBs)					
4U1516-56					
(6624)	22.60	10.0	11.0	30.4	0.
4U1700-37					
(6622)	22.84	1.7	1.5	51.7	2.2
4U1956+35					
(820)	21.57	2.5	3.3	2.7	3.1
II. Intermediate mass System					
4U1656+35					
	19.93[b]	5.0	0.15	-0.1	37.5
(3364)	23.11[c]	5.0	0.15	98.7	37.5
	23.7[d]	5.0	0.15	384.4	37.5
(631)	19.6	5.0	0.15	-.1	37.5
(632)	19.6	5.0	0.15	-0.1	37.5
(633)	19.97	5.0	0.15	-0.1	37.5
III. Low-mass Systems (LMXBs)					
4U1617-15					
(826)	21.34	2.0	1.2	1.4	23.8
(9537)	21.61	2.0	1.2	3.0	23.8
(9538)	21.59	2.0	1.2	2.8	23.8
(8338)	21.45	2.0	1.2	2.0	23.8
4U1626-67					
(2845)	21.39	6.0	1.0	1.7	-13.1
4U1636-53					
(710)	21.62	...	1.0	3.8	-4.8
(2844)	21.75	...		4.2	-4.8
(6769)	21.84	...		5.1	-4.8
4U1659-48					
(6623)	21.82	...	3.5	4.9	-4.3
4U1705-44					
(6621)	22.09	...	...	9.3	-2.3
4U1728-16					
(6762)	21.50	8.0	1.0	2.6	9.0
(10367)	21.59	8.0	1.0	2.8	9.0
4U1735-44					
(6764)	21.71	7.0	0.8	3.8	-7.0
4U1813-14					
(6767)	22.17	1.4	2.0	11.7	1.3
4U1837+04					
(6768)	21.92	7.0	1.5	5.8	4.8
(10649)	21.84	7.0	1.5	5.1	4.8
4U2142+38					
(824hi)	21.57	8.0	1.3	2.3	-11.3
(824dp)	21.52	8.0	1.3	1.9	-11.3
(824nd)	21.48	8.0	1.3	2.2	-11.3
IV. Globular Cluster Sources					
4U1728-33					
(6763)	22.17	10.0	11.0	11.2	-0.2
4U1820-30					
(708A)	21.28	8.5	0.8	3.8	-7.9
(708B)	21.30	8.5	0.8	3.2	-7.9
V. Optically Unidentified Sources					
4U1642-45					
(6761)	22.59	...	...	29.7	-0.1
4U1702-36					
(822)	21.69	...	...	12.3	2.7
4U1744-26					
(6765)	22.46	...	...	22.0	0.8
4U1758-20					
(6770)	22.49	...	...	23.6	1.2
4U1758-25					
(2843)	22.30	...	...	15.1	-1.0
4U1811-17					
(6766)	22.26	...	...	13.8	0.1

[a] Source distance and A_v^{opt} taken from BMC83.
[b] Subset of sequence 3364, high state of 35 day cycle as defined in Vrtilek & Halpern 1985.
[c] Subset of sequence 3364, spike state of pre-eclipse dip as defined in Vrtilek & Halpern 1985.
[d] Subset of sequence 3364, nonspike state of pre-eclipse dip as defined in Vrtilek & Halpern 1985.

vatory showed no evidence of Mg and Si edges (VSK88). The signal-to-noise ratios for the majority of these observations are not sufficient to determine the ionization state of the material through measured shifts in edge energies. In Figures 12–46 (*upper panels*) the photon spectra have been plotted with the OGS binned into four resolution elements (1.6 Å); this improves the S/N ratio and allows us to see the absorption edges at the expense of resolution.

4. INDIVIDUAL SOURCES

An atlas of all the observations discussed in this paper is presented in Figures 12–46. These show the MPC and OGS raw count spectra and the corresponding least-squares-fit photon spectra. The data are given as counts (per 0.3 Å, slightly better than a resolution element, for the OGS, and per energy channel for the MPC), uncorrected for spectral response, background, or higher order contributions. The models are simple continua as given by equations (3)–(5); the effects of photoelectric absorption are included as given in equation (2), with the energy-dependent cross sections and elemental abundances from MM83. Parameters for the model fits are listed in Table 3, and sources appear in the order given in Table 3.

Figures 12–46 (*upper panels*) show the photon spectra with the best-fit model superposed. Each OGS point shown represents four resolution elements (1.6 Å); the bars indicate 1 σ

© American Astronomical Society • Provided by the NASA Astrophysics Data System

1991ApJS...76.1127V

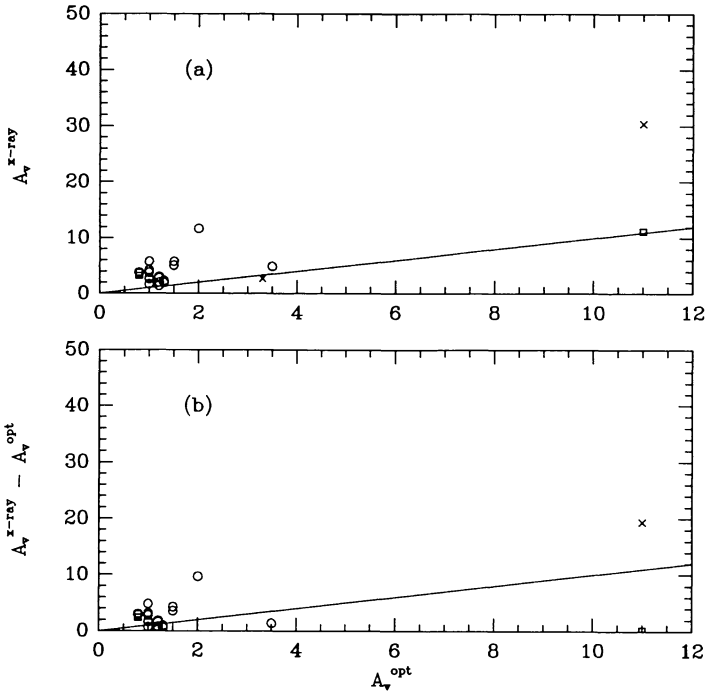

FIG. 6.—(*a*) $A_v^{X\text{-}ray}$ vs. A_v^{opt} as defined in § 3.4. Symbols for the sources are as designated in the legend to Fig. 1. The solid line has a slope of 1. (*b*) The "intrinsic" column density as defined by $A_v^{X\text{-}ray} - A_v^{opt}$ vs. A_v^{opt}. Again the solid line has a slope of 1.

uncertainties. Channel boundaries and 1 σ uncertainties are indicated for the MPC channels by the widths and heights of the crosses, respectively. Note that because of finite channel widths, points shown are not strictly model-independent data points but reflect comparison of data points with the model spectrum. All vertical axes have the same range to facilitate intercomparison of source fluxes, except for the plots of Sco X-1 (which is so bright that we shifted the ordinate by an order of magnitude).

Figures 12–46 (*lower panels*) show the MPC and OGS raw count spectra. MPC counts per energy channel are designated on the left ordinate; OGS counts per 0.3 Å bin and 0.6 Å bin for the 1000 lines mm^{-1} and 500 lines mm^{-1} gratings, respectively, are designated on the right ordinate. The ordinate scales are adjusted to the full range of each spectrum. The abscissa extends to 50 Å for the 1000 lines mm^{-1} grating and to 100 Å for the 500 lines mm^{-1} grating. The counts per energy channel are plotted as solid histograms, the measured background as dashed lines, and the best fit models as solid curves. The "shelf" around 14.8 Å which is prominent in the raw OGS spectra is an instrumental feature due to the nickel coating on the telescope mirror. The most prominent lines observed in the spectra are indicated.

The rest of § 4 comprises comments on each of the 22 sources in the survey.

4.1. *4U 1516−56 (HMXB Circinus X-1; Figure 12)*

An extremely reddened source. A 5000 s OGS observation resulted in no detection. Thus for this source we show only the MPC data. The X-ray column density measured from the MPC alone is 4.0×10^{22} cm^{-2}. Although in four cases comparable or greater column densities were measured where the sources *were* detected in the OGS, the 2–10 keV flux as measured by the MPC was the lowest of all the objects (circled star in Fig. 11); the combination of low flux and high column density explains the lack of a detection in the OGS energy band.

4.2. *4U 1700−37 (HMXB; Figure 13)*

The combined MPC and OGS observations gave one of the highest column densities measured ($N_H = 6.9 \times 10^{22}$ cm^{-2}). No continuum emission is detected in the OGS. The apparent line features in Figure 13 are at a significance below 3 σ.

4.3. *4U 1956+35 (HMXB Cygnus X-1; Figure 14)*

The only massive system observed at sufficient signal-to-noise ratio to detect line features. Cygnus X-1 is also the only black hole candidate observed using the OGS. A detailed paper

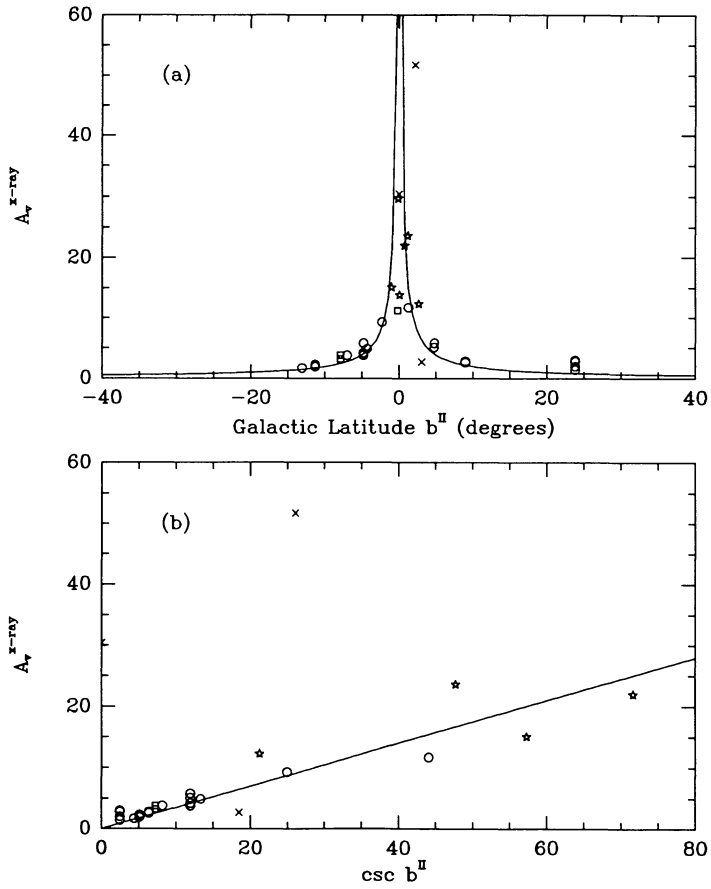

FIG. 7.—(*a*) $A_v^{X\text{-}ray}$ derived from X-ray data using the conversion formula from Heiles, Stark, & Kulkarni (1981) as a function of Galactic latitude b. The solid line represents the cosecant law which was used to fit the data points; where multiple values exist for a given source, only the lowest measured value was used; points near $b = 0.0$ were not used in the fit. Symbols for the sources are as designated in the legend to Fig. 1. (*b*) $A_v^{X\text{-}ray}$ vs. the cosecant of Galactic latitude. The solid line represents the best linear fit with a correlation coefficient $r = 0.62 \pm 0.1$.

© American Astronomical Society • Provided by the NASA Astrophysics Data System

1991ApJS...76.1127V

TABLE 5

SPECTRAL PARAMETERS FOR FITS WITH ANOMALOUS ABUNDANCES OF O, C, AND N

Source	Model type[a] and sequence	A (cm^{-2} s^{-1} keV^{-1})	kT or α[b]	log N_H (cm^{-2})	χ^2_ν and dof[c]	(O/H)	(N/H)	(C/H)
I. Massive (HMXBs)								
4U1956+35 Cyg X-1	PL(820)	1.39±0.13	-1.33±0.42	21.10±0.26	1.4(153)	1.35	11.48	14.45
III. Low-mass (LMXBs)								
4U1617-15	TB(826)	36.31±1.59	1.45±0.5	21.08±0.13	2.2(165)	1.29	24.54	0.27
Sco X-1	TB(8338)	27.42±0.31	2.92±2.58	21.07±0.14	2.4(167)	1.86	31.62	0.83
4U1636-53	PL(710)	1.02±2.21	-3.43±7.67	21.67±1.89	1.5(136)	0.71	4.17	3.24
	PL(2844)	0.30±0.59	-2.06±1.63	21.48±1.55	1.9(136)	0.002	0.79	6.17
4U1659-48 GX339-4	TB(6623)	9.10±0.43	1.10±0.49	21.98±0.85	1.1(134)	0.34	0.02	1.32
4U1735-44	TB(6764)	0.38±0.70	8.35±1.7	21.71±0.41	1.1(134)	0.98	0.003	0.13

[a] PL, TB, and BB stand for power-law, thermal bremsstrahlung, and blackbody.
[b] kT (keV) applies to TB and BB models, α to PL.
[c] Numbers in parentheses are the degrees of freedom used to compute values of χ^2_ν.

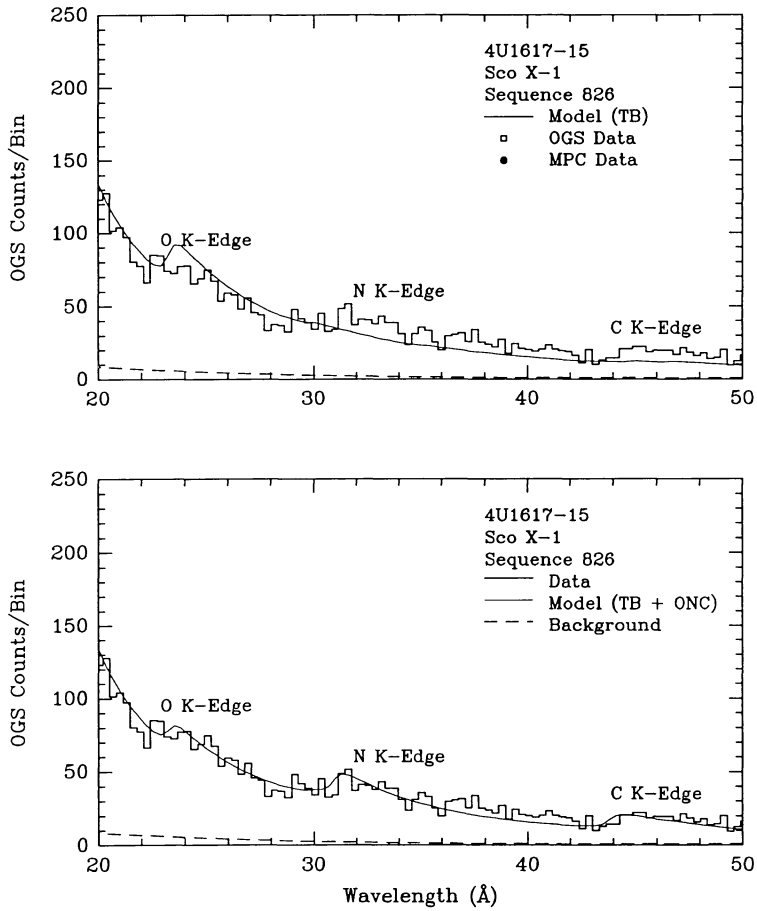

FIG. 8.—The OGS raw count spectra from 20 to 50 Å of Sco X-1 showing the neutral absorption edges of O, N, and C at 43.68 Å, 30.99 Å, and 23.32 Å. *Upper panel:* The simple TB model with the parameters listed in Table 3. *Lower panel:* The TB model with anomalous abundances of O, N, and C as listed in Table 5.

© American Astronomical Society • Provided by the NASA Astrophysics Data System

1991ApJS...76.1127V

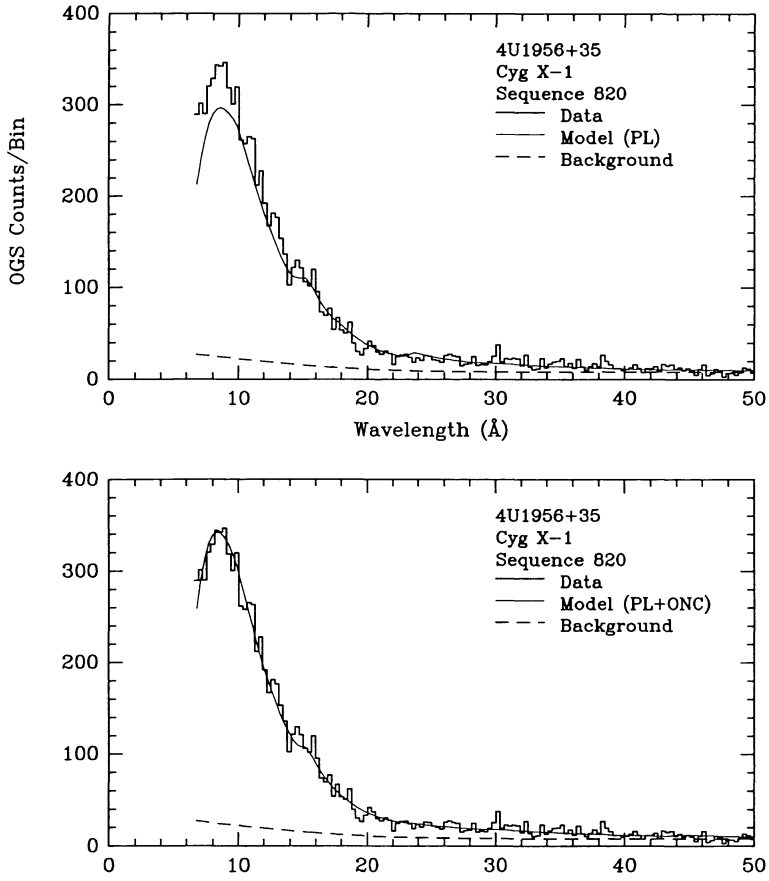

FIG. 9.—OGS raw count spectra of Cyg X-1. *Upper panel:* The simple TB model with the parameters listed in Table 3. *Lower panel:* The TB model with anomalous abundances of O, N, and C as listed in Table 5.

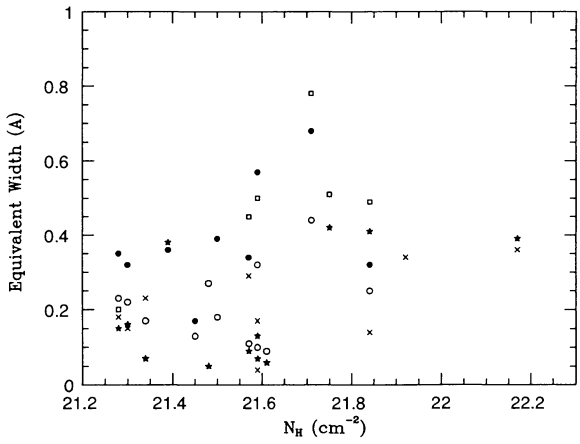

FIG. 10.—Equivalent widths for Fe XXII λ9.0 (*stars*), Fe XXII λ11.8 (*crosses*), Fe XVII λ15.3 (*open circles*), O VIII λ16.0 (*filled circles*), and O VIII λ19.0 (*open squares*), vs. N_H for all the sources.

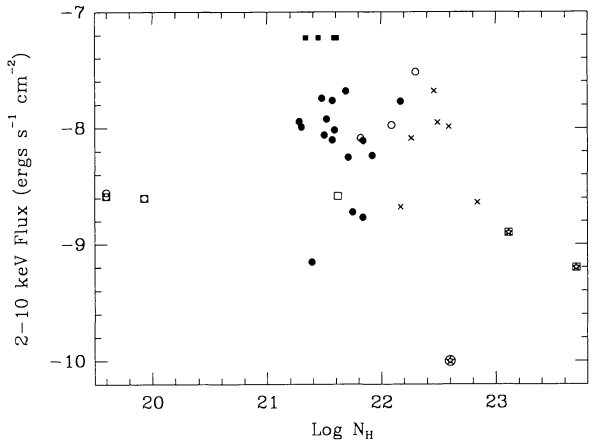

FIG. 11.—X-ray column densities vs. 2–10 keV flux for all observations. The symbols have the following meanings: sources with definitely detected lines (*filled circles*); sources with excess emission, but without sufficient statistics to isolate line features (*open circles*); sources with no detected line emission (*crosses*); sources not detected by the OGS (*stars*), and Sco X-1 (*filled squares*), for which the indicated fluxes are lower limits.

© American Astronomical Society • Provided by the NASA Astrophysics Data System

1991ApJS...76.1127V

© American Astronomical Society • Provided by the NASA Astrophysics Data System

TABLE 6

SUMMARY OF OBSERVED LINE FEATURES

Wavelength (Å)	Possible Identification[a]	Equivalent Width of Feature (Å)[b]									
		Cyg X-1	Sco X-1				1626-67	1636-53		GX9+9	
		820	826	9537	9538	8338	2845	2844	6769	6762	10367
8.4	Fe XXI,Fe XXIII-XXIV	...	0.13±0.04	0.10±0.03	0.10±0.03	0.13±0.04	0.41±0.08	0.17±0.05	...	0.10±0.03	0.08±0.02
9.0,9.6	Fe XXII, Fe XXVI	...	0.07±0.02	0.06±0.02	0.07±0.02	...	0.38±0.10	0.42±0.12	0.41±0.08	...	0.13±0.03
10.2	Fe XVII, Fe XX, Fe XXV	...	...	...	...	...	0.36±0.10	...	0.40±0.10	...	...
11.1	Fe XVII-XVIII,Fe XXIV	0.11±0.02	0.22±0.05	0.07±0.02	...	...	...	0.48±0.12	0.69±0.15	...	...
11.8	Fe XXII-XXIV	...	0.23±0.05	...	0.04±0.01	...	...	...	0.33±0.07	...	0.17±0.05
12.3	Fe XXI-XXII	...	...	...	...	0.09±0.03	0.36±0.09	...	...	...	...
12.8	Fe XX-XXI	0.11±0.02	...	0.07±0.02	...	...	...	0.42±0.10	...	...	...
13.5	Fe XVII-XVIII	...	...	0.09±0.02	...	...	0.42±0.10	...	0.72±0.18	...	...
14.3	Fe XVIII	...	...	...	...	...	...	0.51±0.15	...	...	...
15.3	Fe XVII,O VIII	0.11±0.02	0.17±0.05	0.09±0.03	0.10±0.03	0.13±0.04	...	0.42±0.12	...	0.18±0.05	0.32±0.10
16.0	OVIII, Fe XVIII	...	...	...	...	0.17±0.05	0.36±0.09	...	1.44±0.30	0.39±0.12	0.57±0.15
17.7	OVII,Fe XVI, Fe XXI	...	...	0.13±0.03	...	...	...	...	...	...	...
19.0	O VIII	...	...	...	...	...	...	0.51±0.14	1.51±0.45	...	0.50±0.13
20.5	N VII	...	...	...	...	...	0.60±0.15	0.72±0.20	...	...	...
21.5	O VII	...	...	...	...	...	...	...	...	...	...
24.7	N VII	...	...	...	...	...	...	...	...	...	...
31.0	Si XII	...	...	...	...	...	...	...	...	0.51±0.14	0.48±0.15
42.0	Si IX	...	...	...	...	...	...	...	...	...	...
44.2	Si XII	...	...	...	...	...	...	...	...	...	0.90±0.25

© American Astronomical Society • Provided by the NASA Astrophysics Data System

TABLE 6—*Continued*

Wavelength (Å)	Possible Identification[a]	Equivalent Width of Feature (Å)								
		1735-44	GX17+2	Ser X-1		Cyg X-2		1820-30		GX349+2
		6764	6767	6768	10649	824HI	824ND	708A	708B	822
8.4	Fe XXI,Fe XXIII-XXIV	...	0.19±0.05	0.11±0.03	0.08±0.02	...	...	0.13±0.03	...	0.12±0.03
9.0,9.6	Fe XXII, Fe XXVI	...	0.39±0.10	...	...	...	0.05±0.02	0.15±0.05	0.16±0.05	...
10.2	Fe XVII, Fe XX, Fe XXV	...	...	...	0.13±0.04	0.09±0.03	0.16±0.05	...	0.15±0.03	...
11.1	Fe XVII-XVIII,Fe XXIV	...	...	...	...	...	...	...	...	...
11.8	Fe XXII-XXIV	...	0.36±0.10	0.34±0.10	0.14±0.04	...	...	0.18±0.05	0.15±0.04	...
12.3	Fe XXI-XXII	...	...	...	0.19±0.03	0.29±0.09	0.20±0.06	...	...	0.48±0.15
12.8	Fe XX-XXI	...	...	...	...	...	...	...	...	...
13.5	Fe XVII-XVIII	0.36±0.10	...	...	...	0.27±0.08	...	...	...	....
14.3	Fe XVIII	0.51±0.15	...	...	0.34±0.10	...	...	...	...	...
15.3	Fe XVII,O VIII	0.44±0.10	...	...	0.25±0.08	0.21±0.06	0.27±0.08	0.23±0.06	0.22±0.06	...
16.0	OVIII, Fe XVIII	0.68±0.11	...	...	0.32±0.09	0.34±0.10	...	0.35±0.10	0.32±0.10	...
17.7	OVII,Fe XVI, Fe XXI	0.60±0.10	...	...	0.49±0.15	0.10±0.03	...	...	...	...
19.0	O VIII	0.78±0.10	...	...	0.49±0.15	0.45±0.12	...	0.20±0.06	...	...
20.5	N VII	...	...	...	...	...	...	...	...	...
21.5	O VII	...	...	...	...	...	...	...	0.33±0.10	...
24.7	N VII	...	...	...	...	...	...	0.20±0.07	...	...
31.0	Si XII	...	...	...	...	0.72±0.20	0.40±0.12	...	...	...
42.0	Si IX	0.90±0.25	1.8±0.50	1.44±0.49	...	...	...	...	...	...
44.2	Si XII	0.90±0.26	...	...	0.81±0.20	...	...	...	...	...

[a] From Kato 1976, Raymond & Smith 1977, Doshek & Cowan 1984, and Wiese 1985.
[b] Sources with multiple observations are shown by sequence number.

1991ApJS...76.1127V

TABLE 7

OPTICAL DEPTHS AT NEUTRAL EDGES

Source (Sequence number)	O K-Edge 0.53 keV	Fe L-Edge 0.71 keV	Ne K-Edge 0.87 keV
Cyg X−1:			
(820)	1.5 ± 0.3	0.2 ± 0.1	0.2 ± 0.1
Sco X−1:			
(826)	0.9 ± 0.1	≤0.1	0.3 ± 0.1
(8338)	1.3 ± 0.2	0.3 ± 0.1	0.2 ± 0.1
(9537)	1.6 ± 0.2	0.3 ± 0.1	0.2 ± 0.1
(9538)	1.6 ± 0.2	0.4 ± 0.1	0.2 ± 0.1
KZ TrA:			
(2845)	0.8 ± 0.1	≤0.1	≤0.1
V801Ar:			
(2844)	1.4 ± 0.2	0.3 ± 0.1	≤0.1
(710)	1.3 ± 0.2	0.2 ± 0.1	0.2 ± 0.1
(6769)	2.7 ± 0.4	0.4 ± 0.1	0.3 ± 0.1
GX 339−4:			
(6623)	2.6 ± 0.3	0.4 ± 0.1	0.3 ± 0.1
GX 9+9:			
(6762)	2.8 ± 0.3	0.3 ± 0.1	0.4 ± 0.2
(10367)	1.6 ± 0.2	0.2 ± 0.1	0.2 ± 0.1
V926 Sco:			
(6764)	2.2 ± 0.3	0.2 ± 0.1	0.2 ± 0.1
Ser X−1:			
(6768)	2.9 ± 0.4	0.3 ± 0.1	0.5 ± 0.2
(10649)	3.0 ± 0.3	0.4 ± 0.1	0.3 ± 0.1
Cyg X−2:			
(824HI)	1.4 ± 0.2	≤0.1	≤0.1
(824ND)	1.4 ± 0.2	≤0.1	≤0.1
(824DP)	1.4 ± 0.2	≤0.1	≤0.1
1820−30:			
(708A)	0.9 ± 0.1	≤0.1	≤0.1
(708B)	0.8 ± 0.1	≤0.1	≤0.1

on these results will be presented by Freeman et al. (1991). Cygnus X-1 is known to exhibit high and low states with measured photon energy indicies of ~0.7 in the low states and ~2–5 in the high state. Our observations with a photon energy index of 1.75 are consistent with a high state. We also see no compelling evidence for an excess soft component as has been reported by Pravdo et al. (1980) during the low states; if such a component had been present, the OGS would have detected it. The fits were significantly improved when the abundances of O, N, and C (relative to H) were varied. No significant deviation in O abundance was observed, but a factor of 10 increase in both N and C were inferred (Table 5; Fig. 9, *lower panel*).

4.4. *4U 1656+35 (IMXB Hercules X-1; Figures 15–18)*

The OGS observations of Her X-1 have been analyzed by McCray et al. (1982) and by Vrtilek & Halpern (1985). McCray et al. found no distinct emission or absorption features with the possible exception of broad emission near 1 keV. They noted that the OGS data are consistent with an excess soft component radiating as a blackbody at 0.13 keV. Using pulse-phase spectroscopy, they detected a 240° lag in the phase of pulses at low energies (<0.85 keV) relative to the phase of those at high energies; they interpreted the soft X-rays as reprocessing of the hard X-ray beam at the magnetospheric boundary of the neutron star. Vrtilek & Halpern found that the pre-eclipse dips observed in Her X-1 were punctuated by spikes when the source showed nearly its full X-ray luminosity. By combining OGS and MPC data they were able to show that the excess emission found by McCray et al. near 1 keV was in fact due to the tail end of the power-law emission of the hard source. Vrtilek and Halpern were able to fit all three states (high state, dips, and spikes) with the same flat power law with an absorber of varying covering fraction. Her X-1 showed both the lowest value ($N_H = 4.0 \times 10^{19}$ cm^{-2} at binary phase 0.5 with a covering fraction of 0) and the highest value ($N_H = 5.0 \times 10^{23}$ cm^{-2} at binary phase 0.75 with a covering fraction of greater than 90%) of column density measured in this study. The soft component is consistent with a blackbody at the same temperature found by McCray et al. (1982). We note that there is some evidence for line emission but only the one observation with the 1000 lines mm^{-1} grating (sequence 631) has sufficient resolution to locate individual line features (Fig. 16); as this sequence had some telemetry problems, we did not attempt to identify possible line features.

4.5. *4U 1617−15 (LMXB Scorpius X-1; Figures 19–22)*

The OGS observations of Sco X-1 have been previously analyzed and published (KSC84). They have also been discussed in VSK88 and KVK89. For uniformity, we have reanalyzed these spectra. The main difference between our treatment and that of KSC84 is that we used the absorption models and abundances of MM83 rather than those of Brown & Gould (1970). MM83 include iron, several other (though less important) elements, and the L-absorption feature for all elements. Also, MM83 used updated atomic cross sections from the compilation of Henke et al. (1982), and abundances from Anders & Ebihara (1982). Our results confirm that N is overabundant (Table 5; Fig. 8, *lower panel*), but we do not confirm the apparent underabundance of O reported by KSC84. However, we note that the cosmic abundance for O used by MM83 is 20% less than that given by Brown & Gould (1971).

The telemetry alloted to the MPC was saturated during pointings at Sco X-1 because of the source's extreme brightness; accordingly, we used the OGS data alone for the spectral fits. We were thus unable to constrain the temperature: in the four separate observations, temperature and normalization show strong inverse correlation and are poorly determined individually. Even with the small effective area of the OGS, Sco X-1 is so bright that the zero order saturated the telemetry allotted to the HRI. In all but one case (seq. 826) the source was examined using an offset position such that the zero-order did not fall on the HRI. This results in a considerable improvement in statistical quality of the first order, but there is an uncertainty in the location of the zero order of 0.3 Å, or slightly under one resolution element, resulting in a corresponding uncertainty on the wavelength scale of the first order.

The line equivalent widths we measure are consistent with those of KSC84. The influence of the spectral lines detected in the OGS on the *Einstein* SSS spectra was demonstrated by VSK88: in analyzing *Einstein* SSS spectra of Sco X-1, VSK88 included the strongest lines detected in the OGS (as determined by equivalent width) in a simple model. In each case the line energies were held constant at their measured OGS value and the line strengths allowed to vary. In every case the re-

© American Astronomical Society • Provided by the NASA Astrophysics Data System

1991ApJS...76.1127V

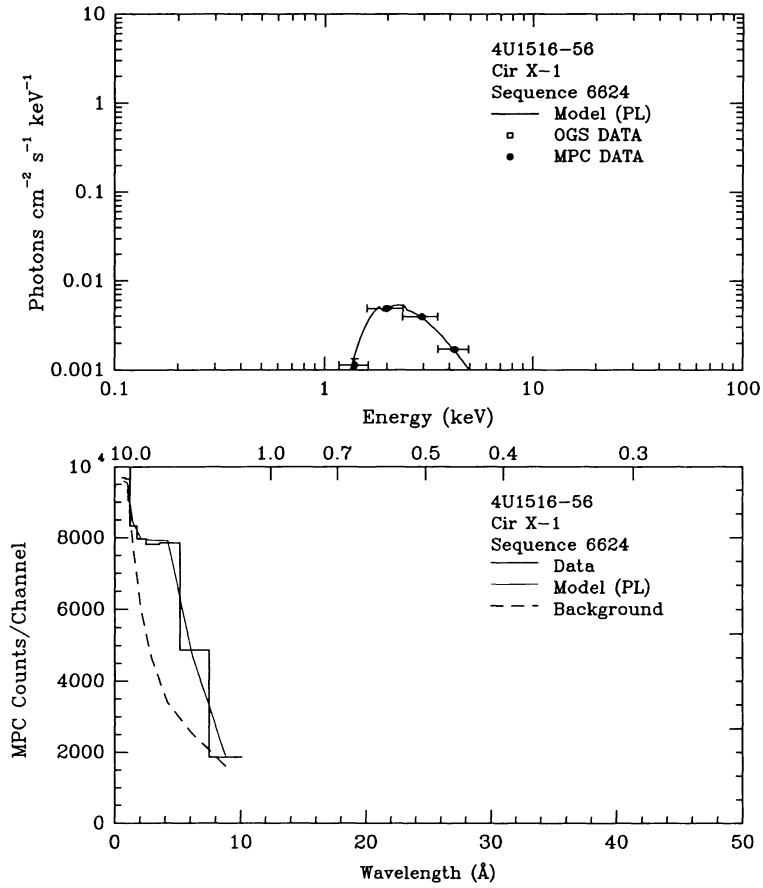

FIG. 12.—As noted in Fig. 5 for 4U 1516−56. There was no detection in the OGS so only MPC data are shown.

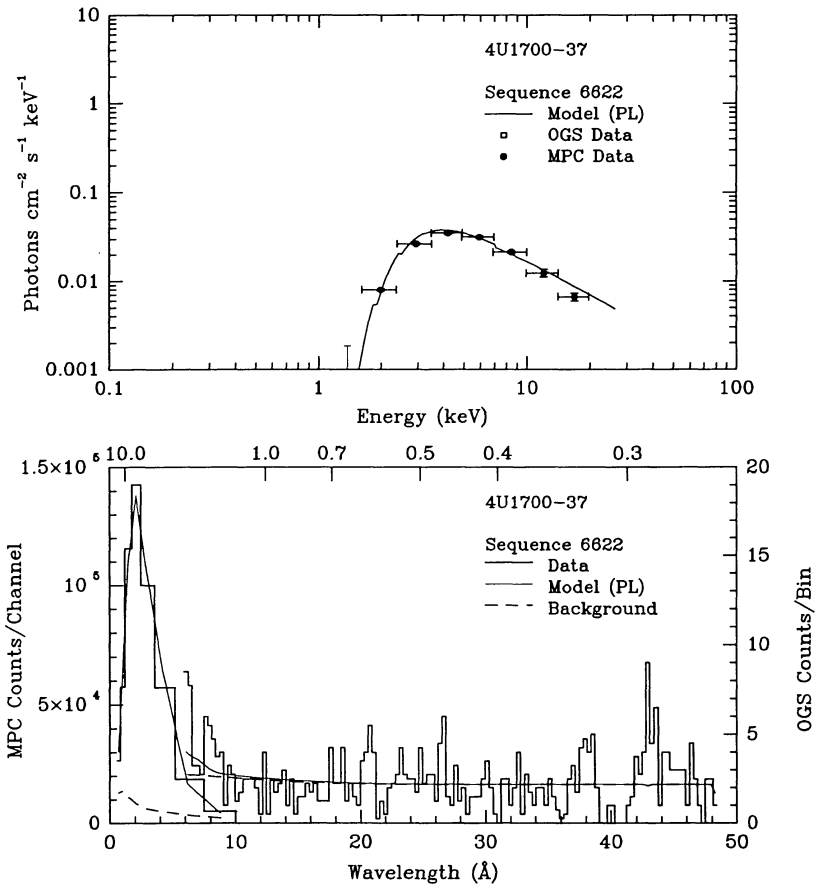

FIG. 13.—As noted in Fig. 5 for 4U 1700−37

© American Astronomical Society • Provided by the NASA Astrophysics Data System

1991ApJS...76.1127V

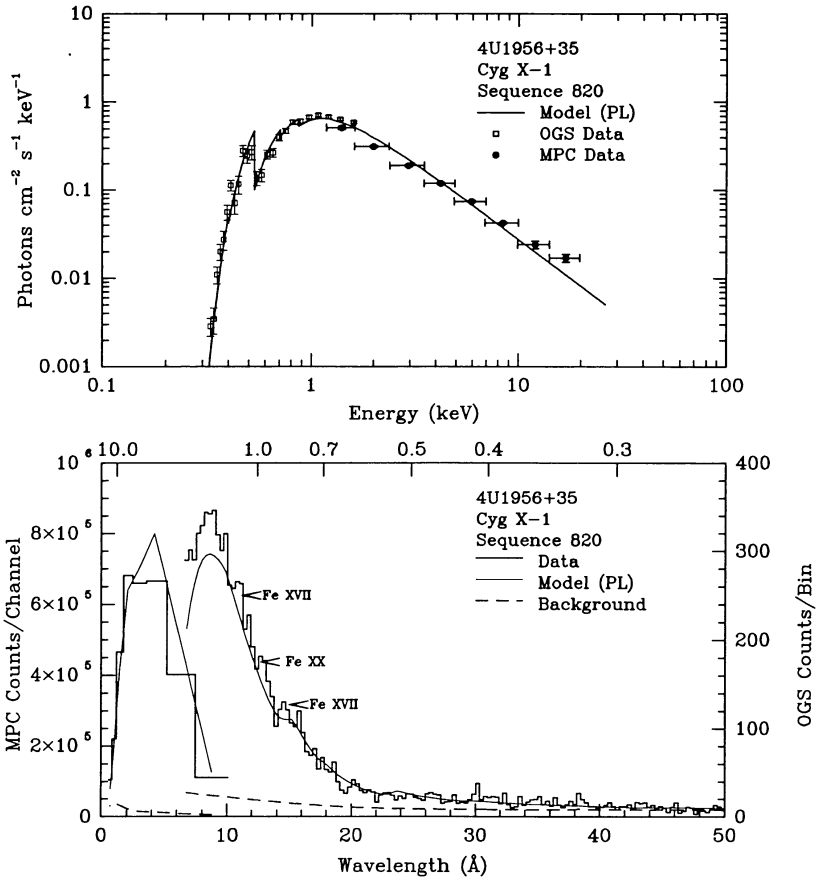

FIG. 14.—As noted in Fig. 5 for 4U 1956+35

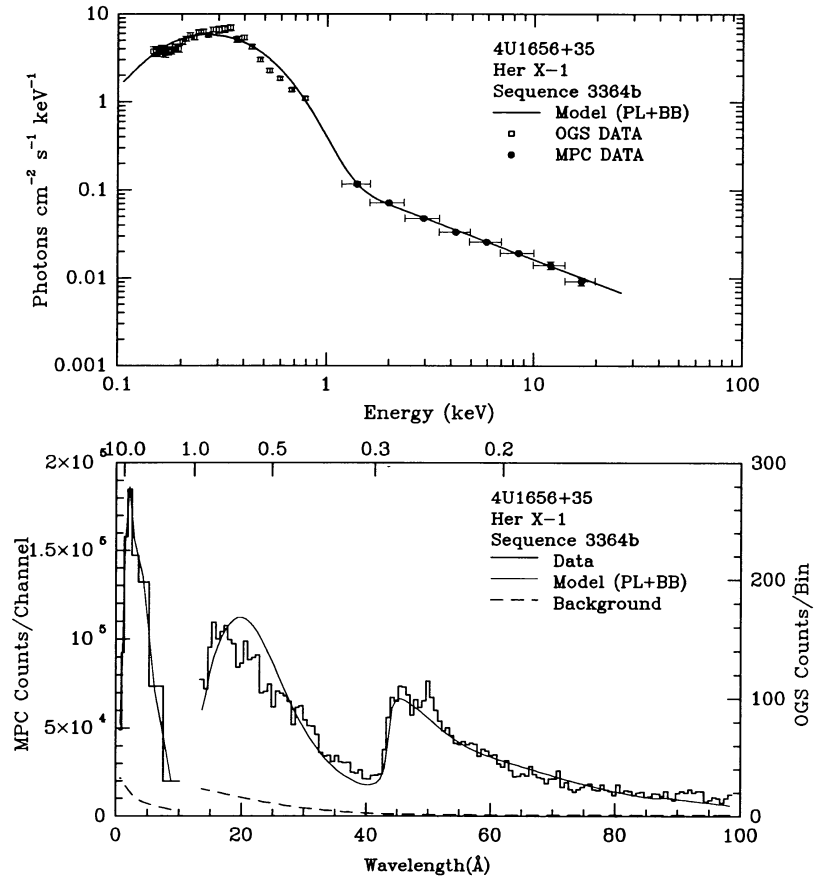

FIG. 15.—As noted in Fig. 5 for 4U 1656+35. High state of sequence 3364. 500 lines mm^{-1} grating.

© American Astronomical Society • Provided by the NASA Astrophysics Data System

1991ApJS...76.1127V

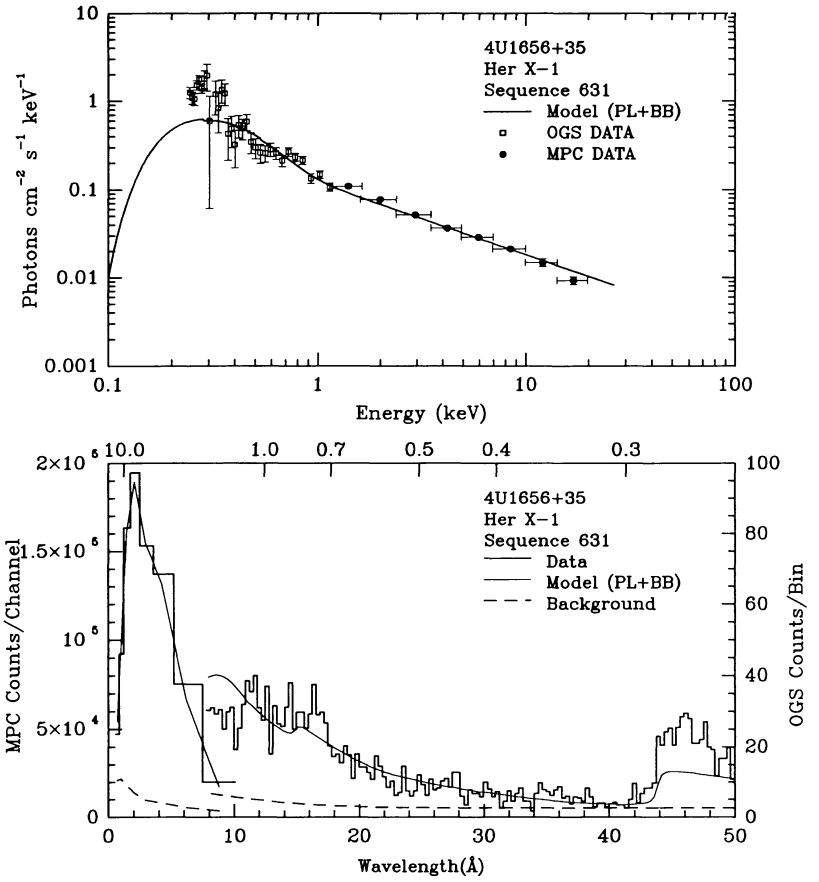

FIG. 16.—As noted in Fig. 5 for 4U 1656+35. Sequence 631. 1000 lines mm^{-1} grating.

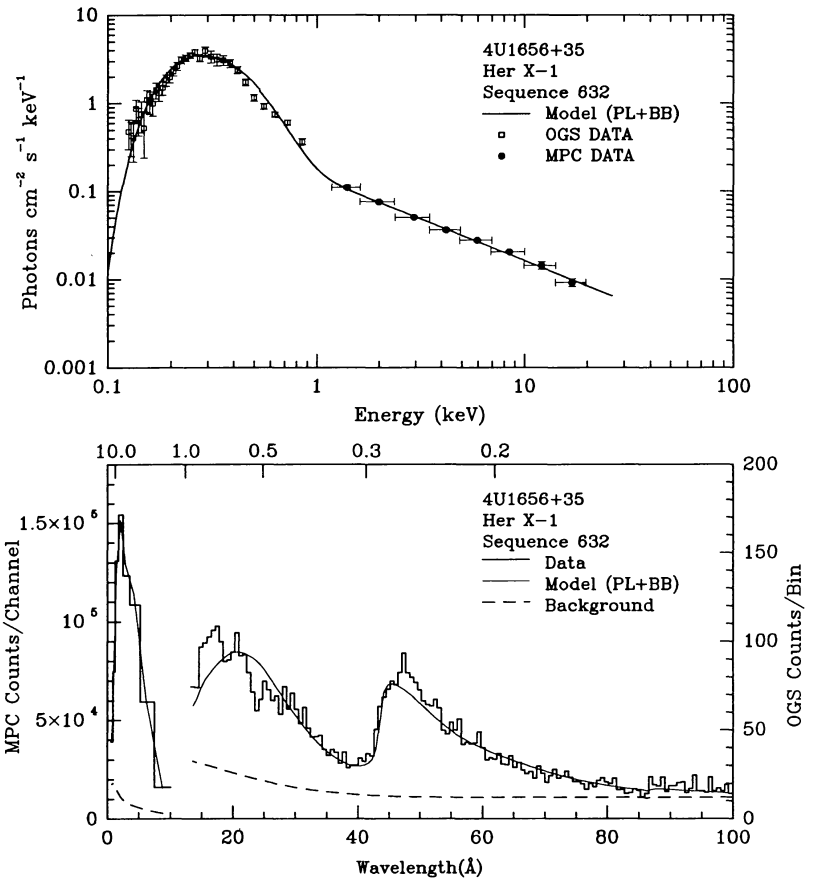

FIG. 17.—As noted in Fig. 5 for 4U 1656+35. Sequence 632. 500 lines mm^{-1} grating.

© American Astronomical Society • Provided by the NASA Astrophysics Data System

1991ApJS...76.1127V

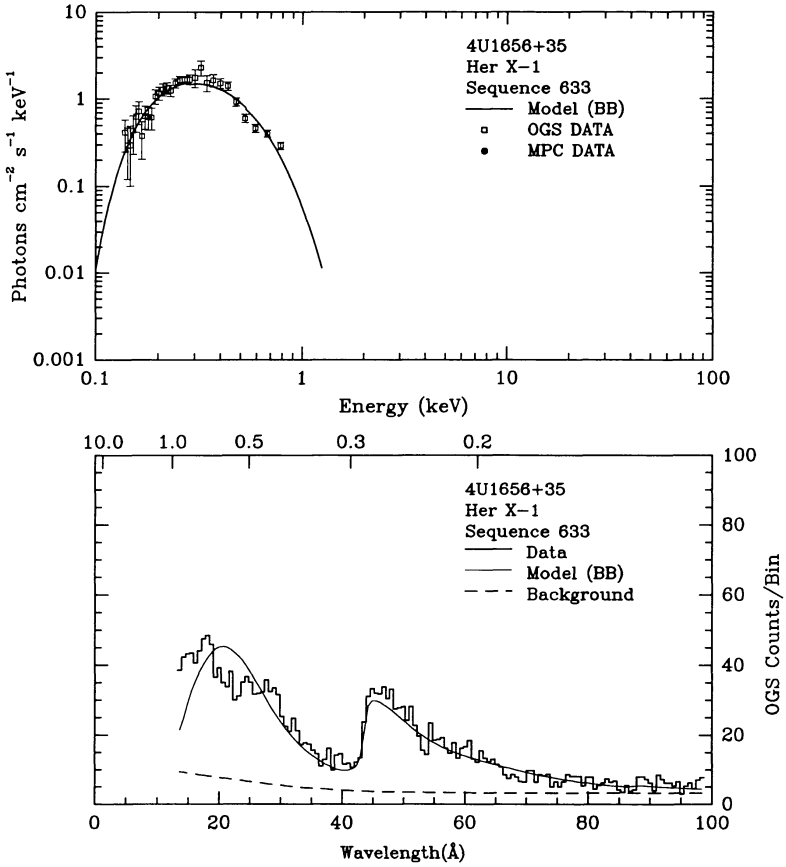

FIG. 18.—As noted in Fig. 5 for 4U 1656+35. Sequence 633. 500 lines mm^{-1} grating. MPC data for this observation were obtained but are now unavailable.

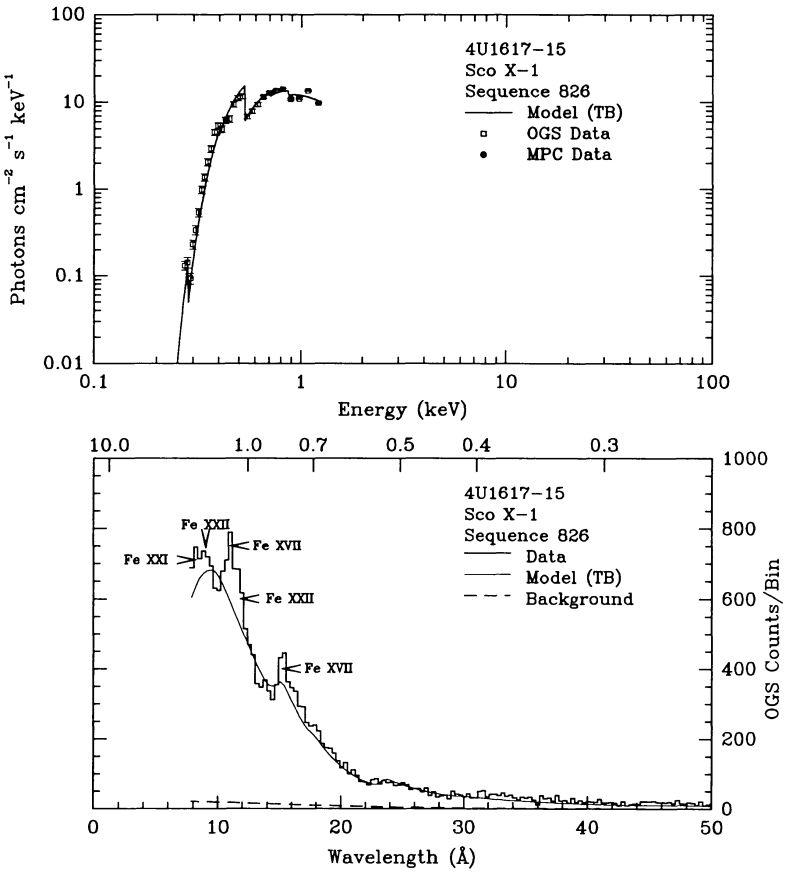

FIG. 19.—As noted in Fig. 5 for 4U 1617−15. Sequence 826.

© American Astronomical Society • Provided by the NASA Astrophysics Data System

1991ApJS...76.1127V

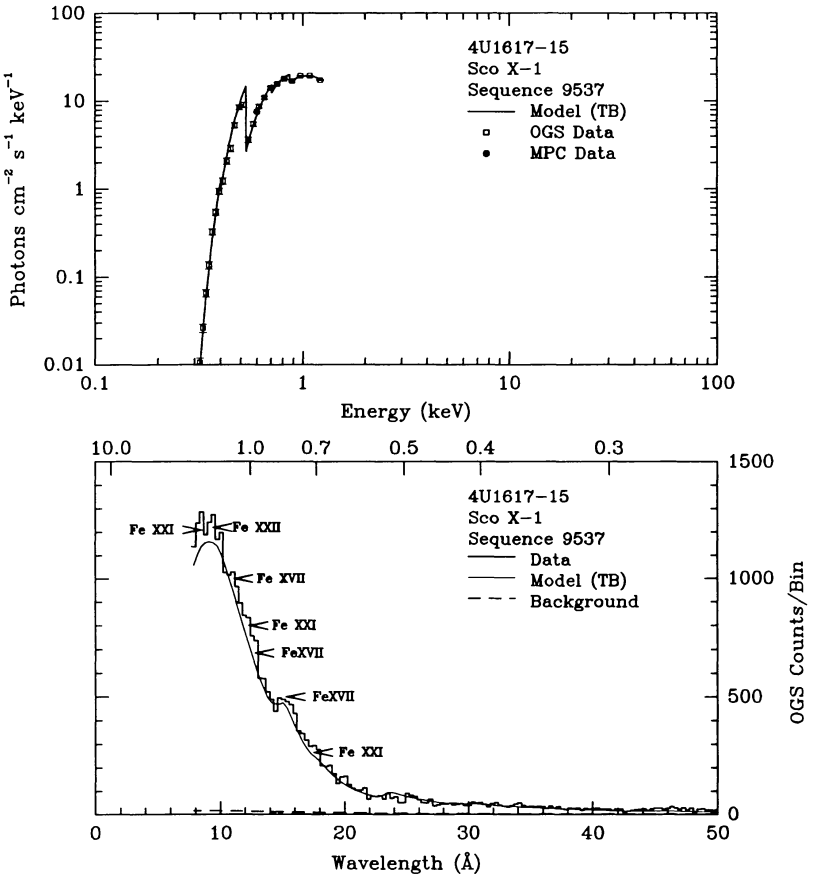

FIG. 20.—As noted in Fig. 5 for 4U 1617−15. Sequence 9537.

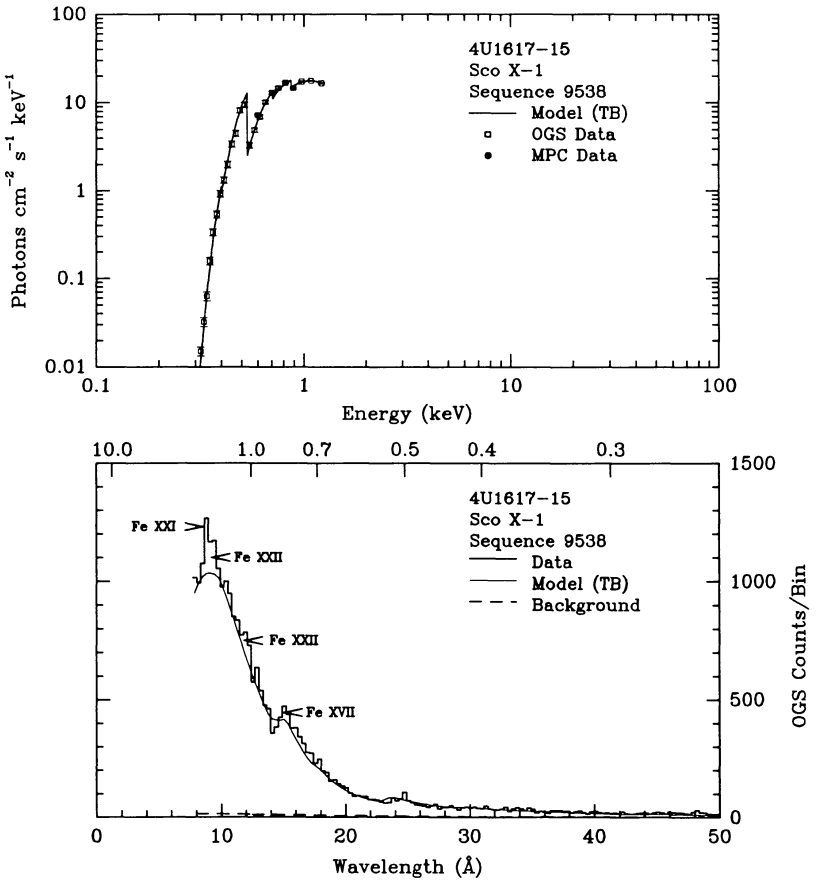

FIG. 21.—As noted in Fig. 5 for 4U 1617−15. Sequence 9538.

© American Astronomical Society • Provided by the NASA Astrophysics Data System

1991ApJS...76.1127V

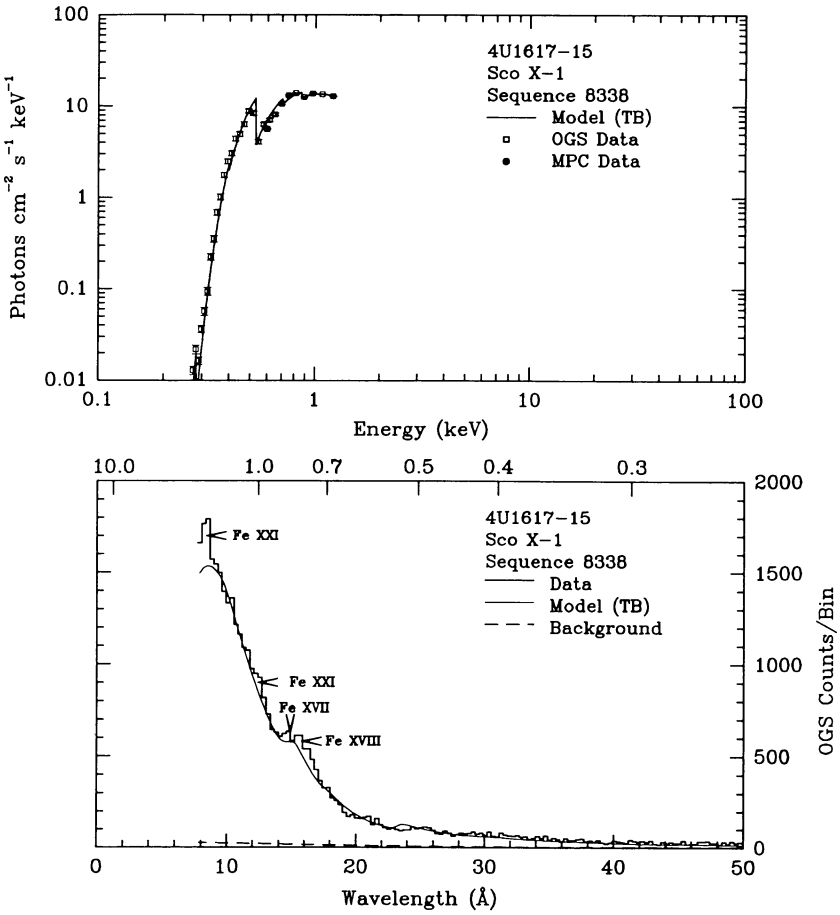

FIG. 22.—As noted in Fig. 5 for 4U 1617−15. Sequence 8338.

duced χ^2 decreased significantly when the OGS lines were added. The significance of the reduction in χ^2 with the addition of free parameters was tested with the application of an *F*-test. In all cases the probability of obtaining the observed reduction in χ^2 by chance is less than 0.1%.

EXOSAT TGS observations confirm the presence of line emission between 10 and 20 Å (Brinkman et al. 1985). Both *EXOSAT* and *Einstein* saw prominent lines at 11 Å and at 15–16 Å attributed to Fe XVII during only one of several observations. *EXOSAT* was able to determine that the observation that showed the strong line emission occurred when Sco X-1 was in a flaring state. We suggest that the one OGS sequence in which the same prominent lines features are seen (seq. 826) is also likely to have occurred during an X-ray–flaring state (we cannot confirm this hypothesis since both the MPC and OGS zero-order telemetry were saturated by the high count rates of Sco X-1, precluding temporal analysis).

4.6. *4U 1626−67 (LMXB; Figure 23)*

Emission lines attributable to Fe and N are observed. The line feature observed at 16.2 Å cannot be attributed to O VIII Lyβ since we do not observe a corresponding line from O VIII Lyα at 19.3 Å. The relatively low column density ($N_H = 2.5 \times 10^{21}$ cm^{-2}) but low X-ray intensity makes this source an excellent target for future high resolution instruments with greater sensitivity.

4.7. *4U 1636−53 (LMXB; Figures 24–26)*

There were 3 observations for this source: one which lasted for nearly a full binary orbit (~14,400 s) taken with the 500 lines mm^{-1} grating (Fig. 24), and two which were about half an orbit apiece taken with the 1000 lines mm^{-1} grating (Figs. 25–26). Although we have two observations that cover roughly half an orbit apiece, the empheris is not well enough known for us to determine which half is covered. Thus we cannot determine if the differences between the lines detected in the two observations are due to orbital position or changes in source state. The 19.3 Å feature attributable to O VIII Lyα was stronger than the 16.2 Å feature attributable to O VIII Lyβ as is expected for a coronal (collisionally ionized) source. The 2–10 keV fluxes ranged from 1.5×10^{-9} ergs cm^{-2} s^{-1} to 2.6×10^{-9} ergs cm^{-2} s^{-1}. Line emission was most prominent in the *lowest* flux observation (Fig. 26).

4.8. *4U 1659−48 (LMXB GX339−4; Figure 27)*

Appears very similar to Sco X-1 in that line features appear to be present at 11 Å and 15 Å but are below 3 σ significance. Another excellent candidate for future instruments with higher sensitivity.

© American Astronomical Society • Provided by the NASA Astrophysics Data System

1991ApJS...76.1127V

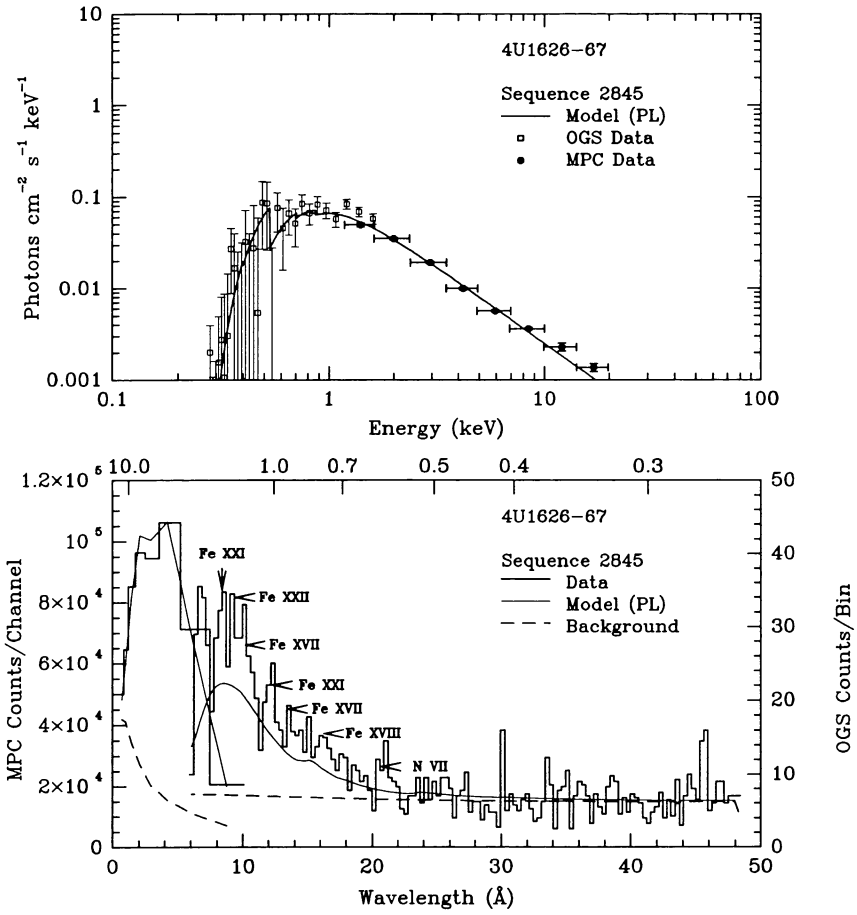

FIG. 23.—As noted in Fig. 5 for 4U 1626−67

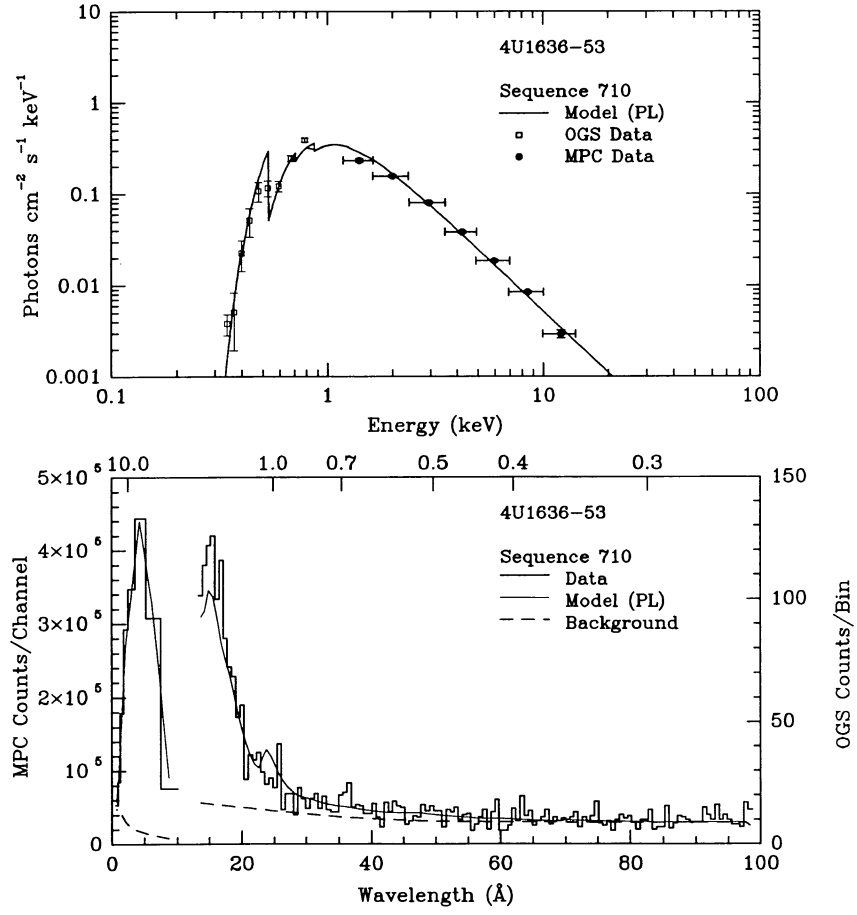

FIG. 24.—As noted in Fig. 5 for 4U 1636−53. Sequence 710. 500 lines mm^{-1} grating.

© American Astronomical Society • Provided by the NASA Astrophysics Data System

1991ApJS...76.1127V

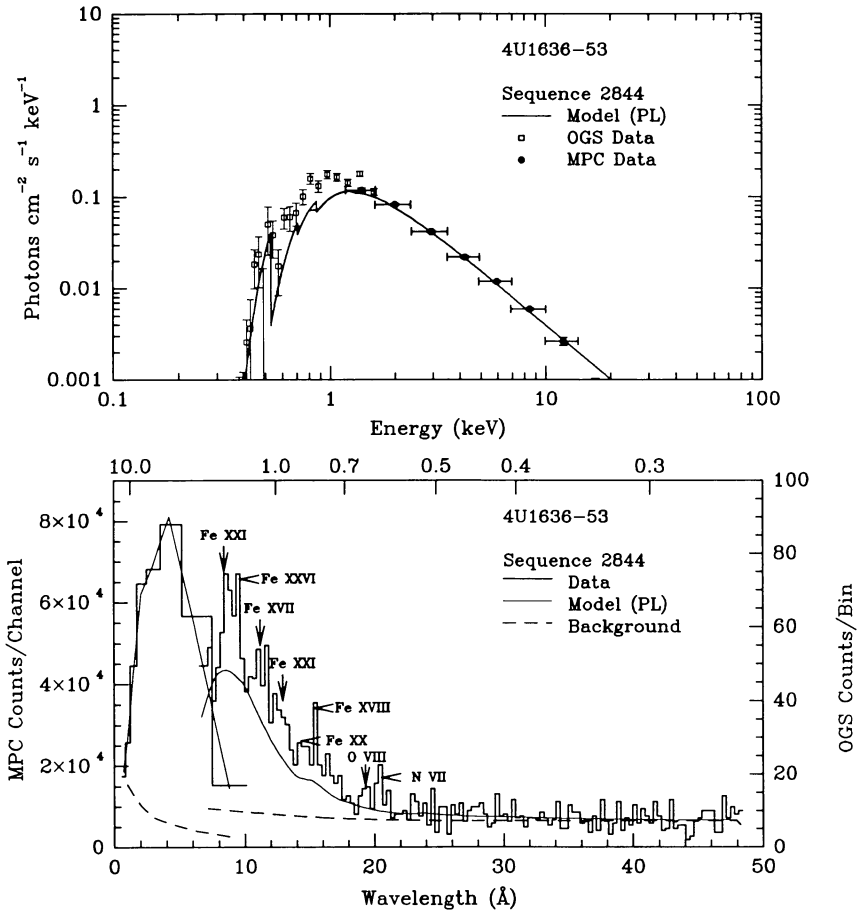

FIG. 25.—As noted in Fig. 5 for 4U 1636−53. Sequence 2844.

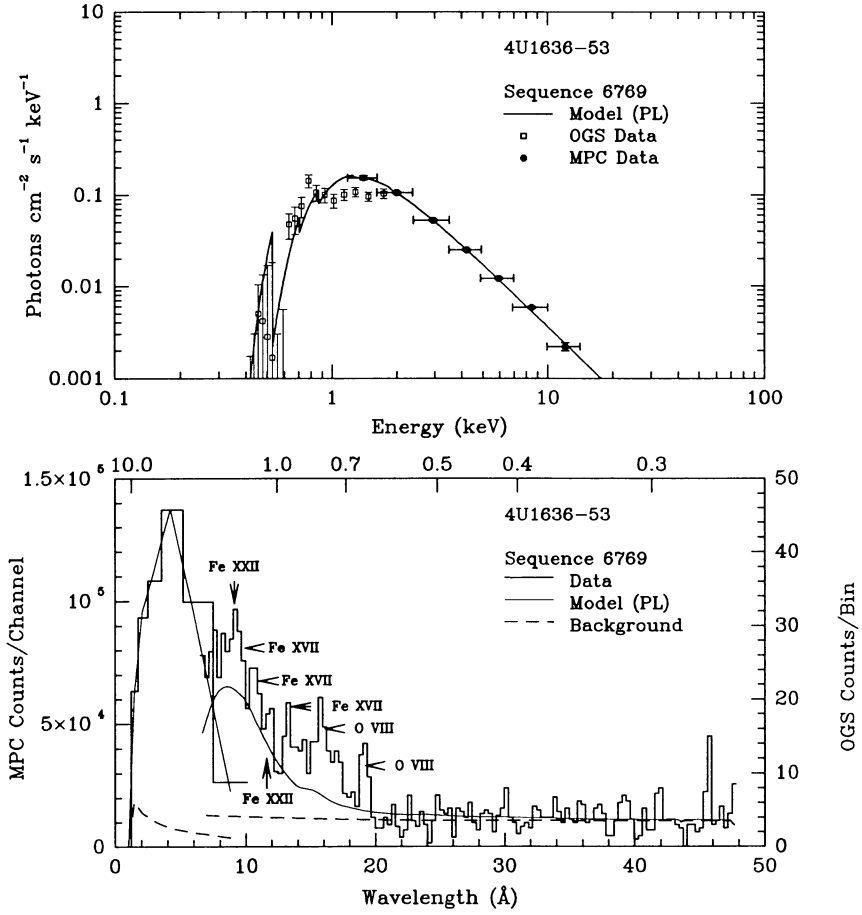

FIG. 26.—As noted in Fig. 5 for 4U 1636−53. Sequence 6769.

© American Astronomical Society • Provided by the NASA Astrophysics Data System

1991ApJS...76.1127V

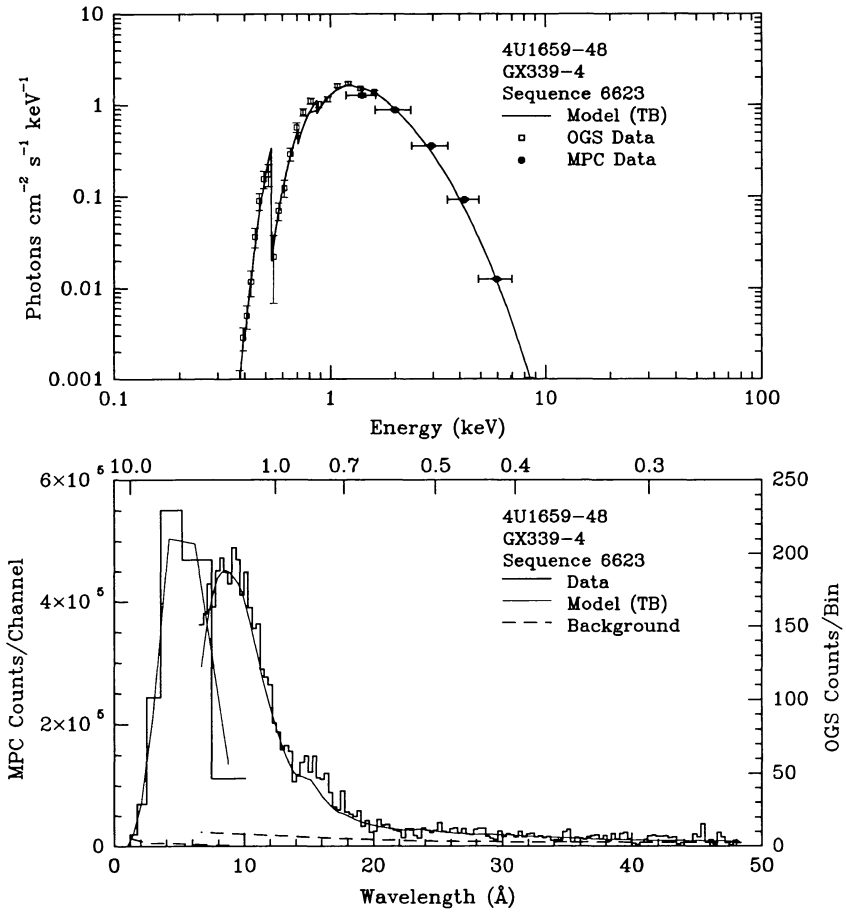

FIG. 27.—As noted in Fig. 5 for 4U 1659–48

4.9. *4U 1705–44 (LMXB; Figure 28)*

No line features were detected with a significance greater than 3 σ.

4.10. *4U 1728–16 (LMXB GX9+9; Figures 29–30)*

The OGS and MPC observations have been analyzed by VRT86a and have been discussed in VSK88, KVK89, and Liedahl et al. (1990). The line feature observed at 16.2 Å cannot be attributed to O VIII Lyβ since we either do not observe a corresponding line from O VIII Lyα at 19.3 Å (Fig. 29), or we observe one that is weaker than the O VIII Lyβ feature (Fig. 30). In addition, VRT86a noted that the line feature observed at 15 Å is inconsistent with an interpretation of the 16.2 Å feature as Fe XVII emission from a hot coronal plasma; Liedahl et al. (1990) showed that if the 16.2 Å feature is identified as Fe XIX $3s$–$2p$, then the simultaneous appearance of the 15 Å and 16 Å emission is consistent with a cool photoionized region. Model fits to the SSS spectra of this source were significantly improved when lines resolved by the OGS were included (VSK88).

4.11. *4U 1735–44 (LMXB; Figure 31)*

Line features are detected between 10 and 20 Å; using the models of KVK89, we find that they are consistent with emission region temperatures of (6–10) $\times$ 10^7 K. The 19.3 Å feature attributable to O VIII Lyα is stronger that the 16.2 Å feature attributable to O VIII Lyβ as expected for a coronal (collisionally ionized) source.

4.12. *4U 1813–14 (LMXB GX 17+2; Figure 32)*

Although this source has a fairly high column density (N_H = 1.5 $\times$ 10^{22} cvm^{-2}), it was detected in the OGS and a few line features attributable to highly ionized states of Fe (XXI–XXV) were observed. It is similar to 4U 1700–37 in that very little soft continuum emission was present, which implies that we may not be looking directly at the X-ray source. Since transmission at wavelengths greater than 30 Å is less than 10^{-4} for column densities above 10^{22} cm^{-2}, the feature at 42 Å is unlikely to be real.

4.13. *4U 1837+04 (LMXB Serpens X-1; Figures 33–34)*

The OGS and MPS observations have been analyzed by VRT86a and discussed in VSK88 and KVK89. A blend of emission lines attributable to Fe and O are observed and roughly fitted by a collision-dominated ionization model at a temperature of 3 $\times$ 10^6 K. The 19.3 Å feature attributable to O VIII Lyα was stronger that the 16.2 Å feature attributable to O VIII Lyβ as is expected for a coronal (collisionally ionized)

© American Astronomical Society • Provided by the NASA Astrophysics Data System

1991ApJS...76.1127V

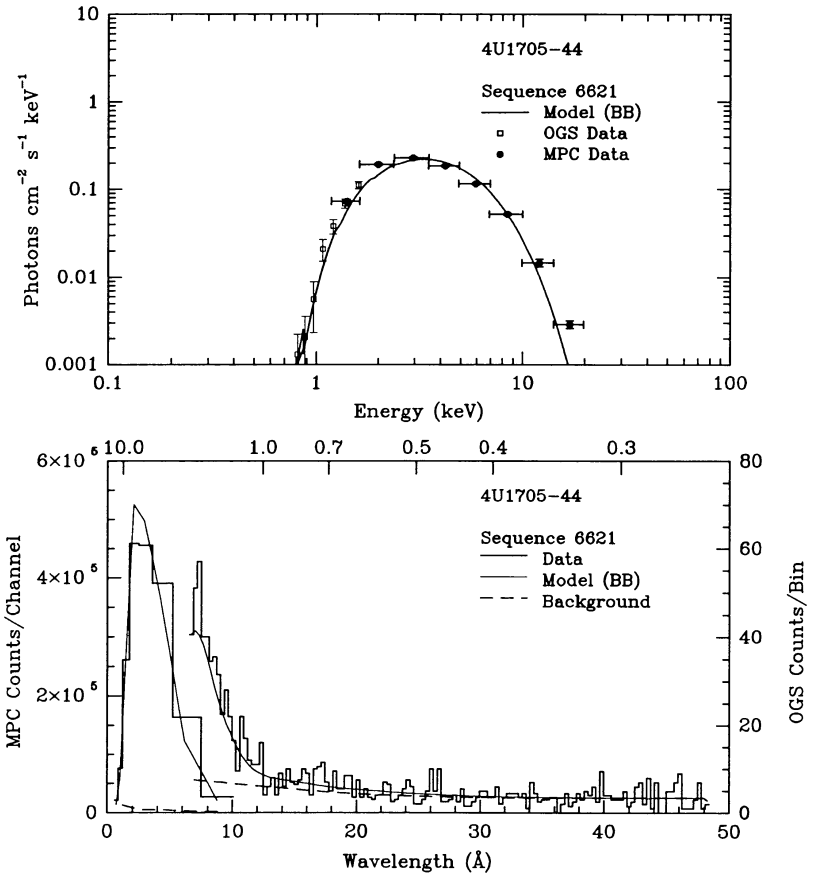

FIG. 28.—As noted in Fig. 5 for 4U 1705−44

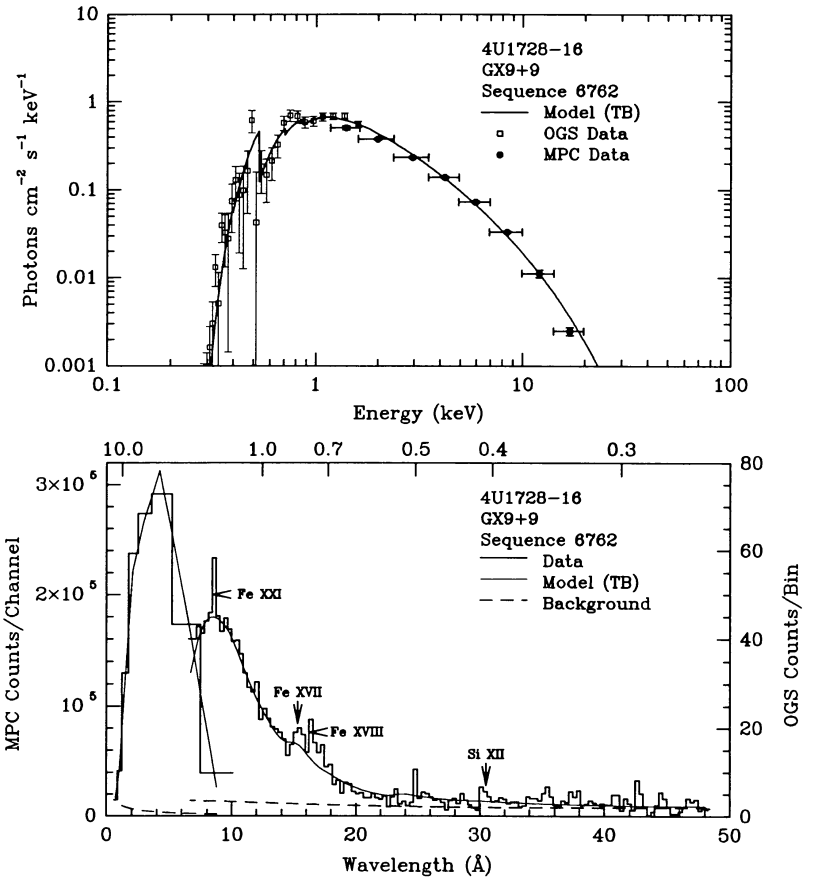

FIG. 29.—As noted in Fig. 5 for 4U 1728−16. Sequence 6762.

© American Astronomical Society • Provided by the NASA Astrophysics Data System

1991ApJS...76.1127V

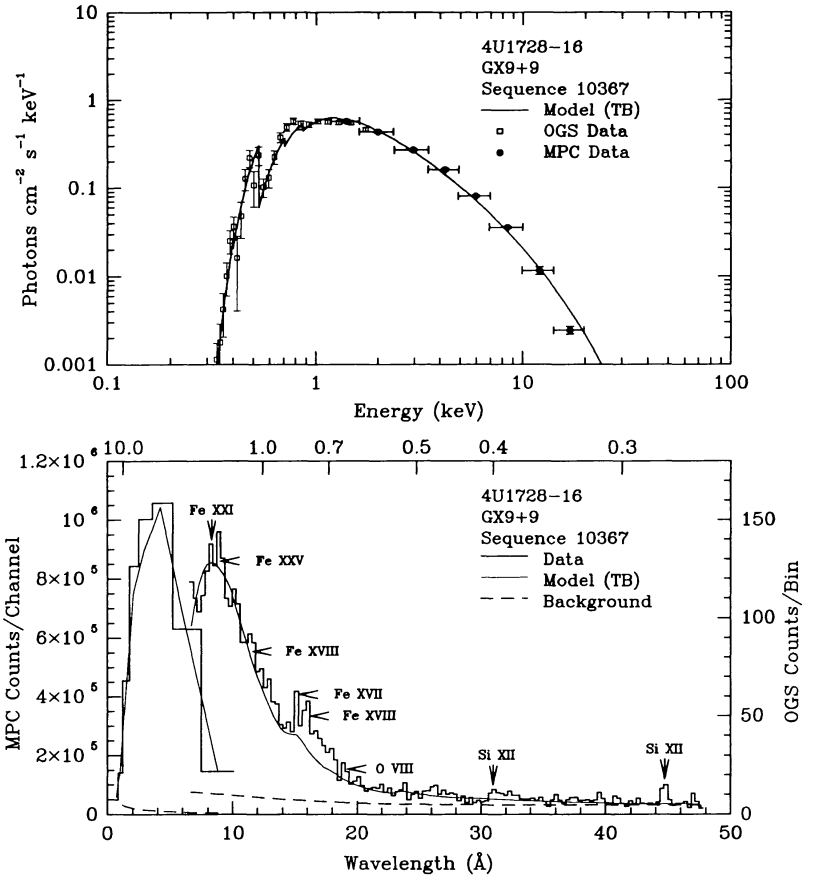

FIG. 30.—As noted in Fig. 5 for 4U 1728−16. Sequence 10367.

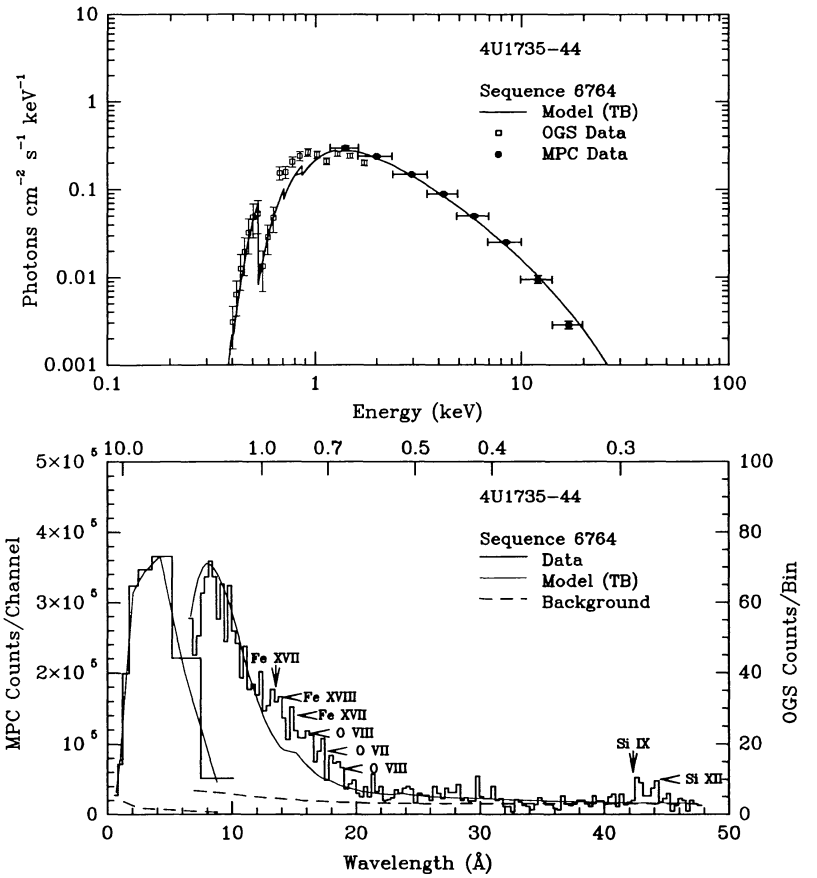

FIG. 31.—As noted in Fig. 5 for 4U 1735−44

© American Astronomical Society • Provided by the NASA Astrophysics Data System

1991ApJS...76.1127V

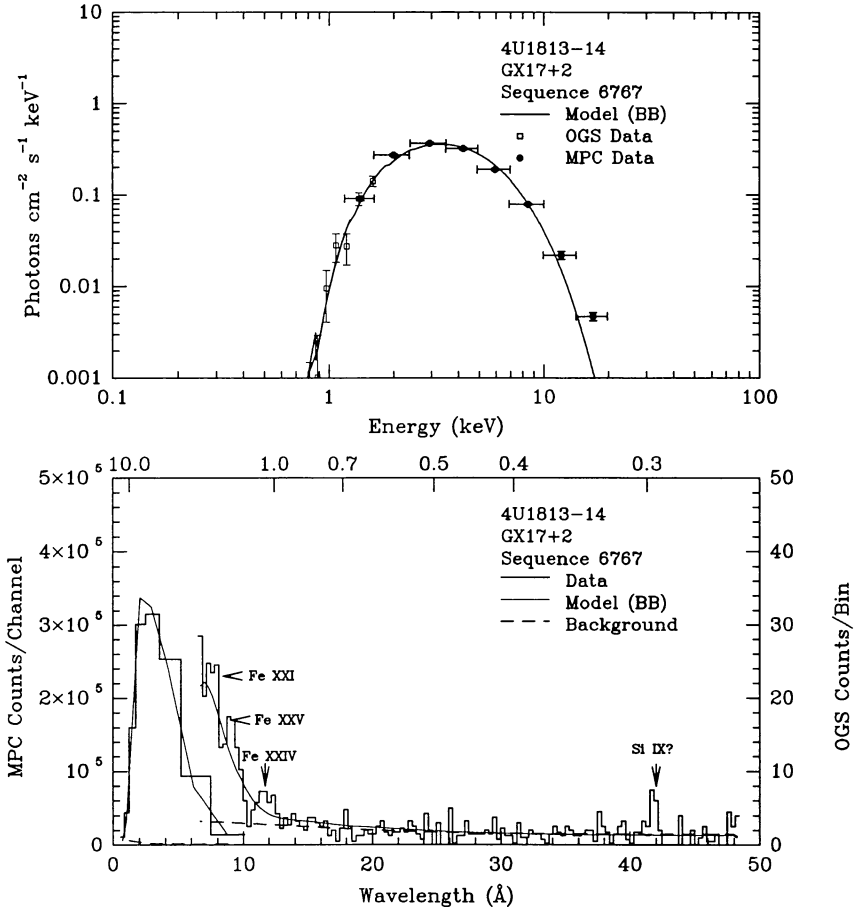

FIG. 32.—As noted in Fig. 5 for 4U 1813−14

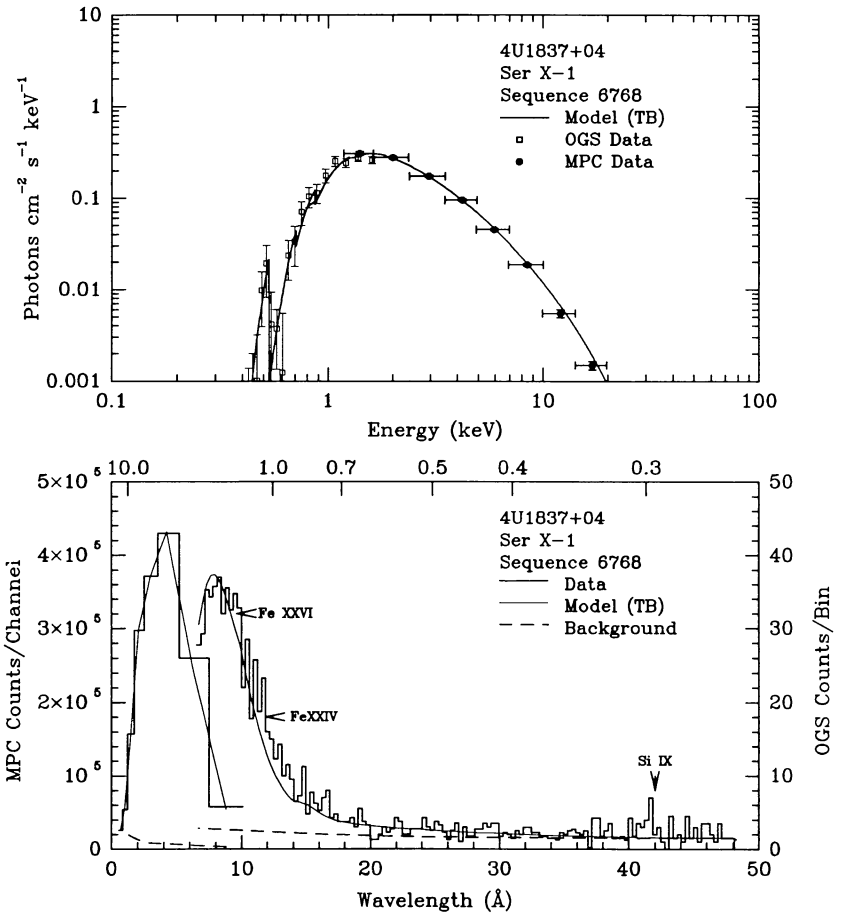

FIG. 33.—As noted in Fig. 5 for 4U 1837+04. Sequence 6768.

© American Astronomical Society • Provided by the NASA Astrophysics Data System

1991ApJS...76.1127V

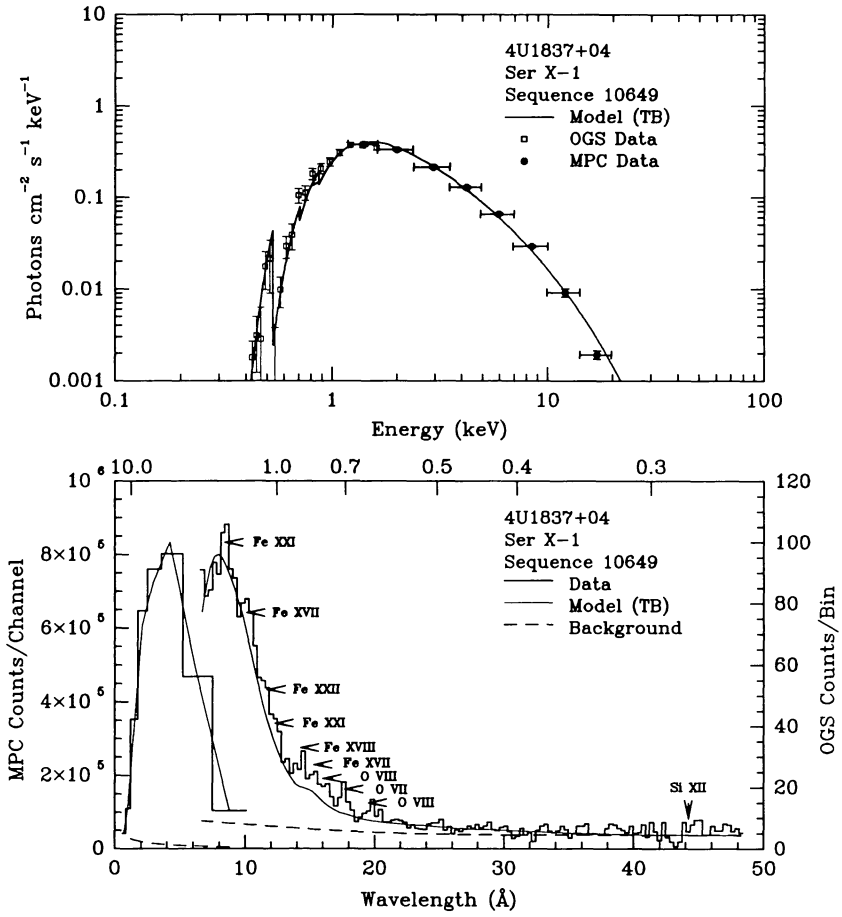

FIG. 34.—As noted in Fig. 5 for 4U 1837+04. Sequence 10649.

source. Model fits to the SSS spectra of this source were also significantly improved when lines resolved by the OGS were included (VSK88).

4.14. *4U 2142+38 (LMXB Cygnus X-2; Figures 35–37)*

The OGS and MPC observations have been analyzed by VRT86b and have been discussed in VSK88, KVK89, and Liedahl et al. (1990). Emission lines attributable to O, Fe, and Si are detected. VRT86b divided this observation into three states: the sum of observed intensity dips, the sum of high states surrounding the dips, and a high state during which no dips were seen to occur. The former two can be associated with the flaring branch of the Z, and the latter with the normal branch. During the flaring branch, line features are observed at 16.2 Å and 19.3 Å which can be attributed to O VIII Lyβ and O VIII Lyα. The 19.3 Å feature is stronger than the 16.2 Å feature as expected for a coronal (collisionally ionized) source. During the normal branch, the O VIII features disappear, but an emission line around 16.0 Å persists and is attributed to Fe XVII. In both cases, the lines can be roughly fitted with a low-density, hot collisional plasma of temperature greater than 5×10^6 K (model of KVK89). The *EXOSAT* TGS detected excess emission (above a thermal bremsstrahlung continuum) between 10 and 20 Å but was unable to distinguish individual line features, probably because of the lower spectral resolution of the instrument (Chiappetti et al. 1990). Model fits to the SSS spectra of this source were also significantly improved when lines resolved by the OGS were included (VSK88).

4.15. *4U 1728–33 (Source in Globular Cluster GX 354–0; Figure 38)*

This source was just barely detected by the OGS, probably owing to its modest 2–10 keV flux (2.1×10^{-9} ergs cm^{-2} s^{-1}) and relatively high column density ($N_H = 1.5 \times 10^{22}$ cm^{-2}).

4.16. *4U 1820–30 (Source in Globular Cluster NGC 6624; Figures 39–40)*

The OGS and MPC observations have been analyzed by VRT86a and have been discussed in VSK88, KVK89, and Liedahl et al. (1990). As noted for GX 9+9 above, the line feature observed at 16.2 Å cannot be attributed to O VIII Lyβ since the corresponding line expected from O VIII Lyα at 19.3 Å is either absent or weak. The simultaneous presence of 15 Å and 16 Å emission is consistent with a cool, photoionized region with the 16 Å emission attributable to the $3s$–$2p$ transition of Fe XIX (Liedahl et al. 1990).

Since the early analysis by VRT86a, Stella, Priedhorsky, & White (1987) found that 1820–30 has a binary period of $\approx$ 600 s. The OGS observation is integrated over 24 binary

© American Astronomical Society • Provided by the NASA Astrophysics Data System

1991ApJS...76.1127V

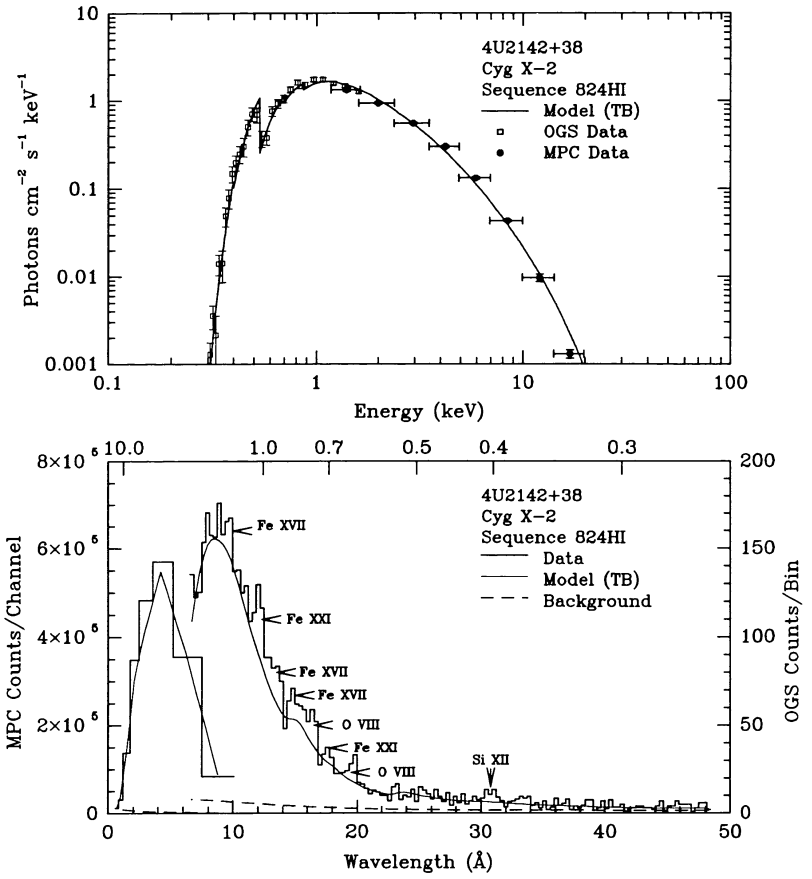

FIG. 35.—As noted in Fig. 5 for 4U 2142+38. High state of sequence 824.

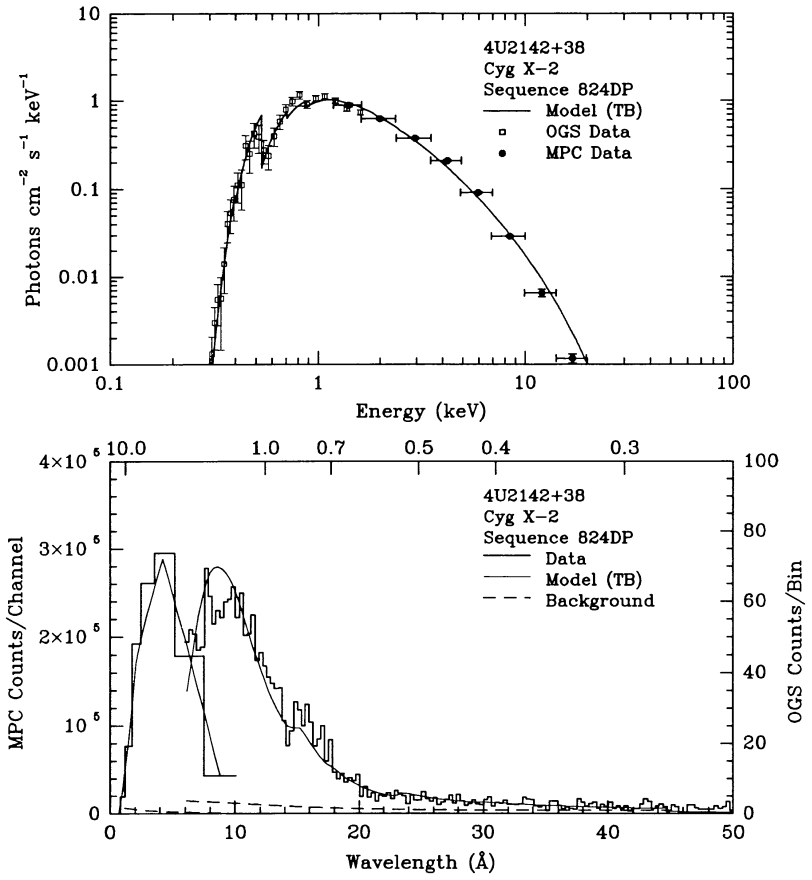

FIG. 36.—As noted in Fig. 5 for 4U 2142+38. Summed dips of sequence 824.

© American Astronomical Society • Provided by the NASA Astrophysics Data System

1991ApJS...76.1127V

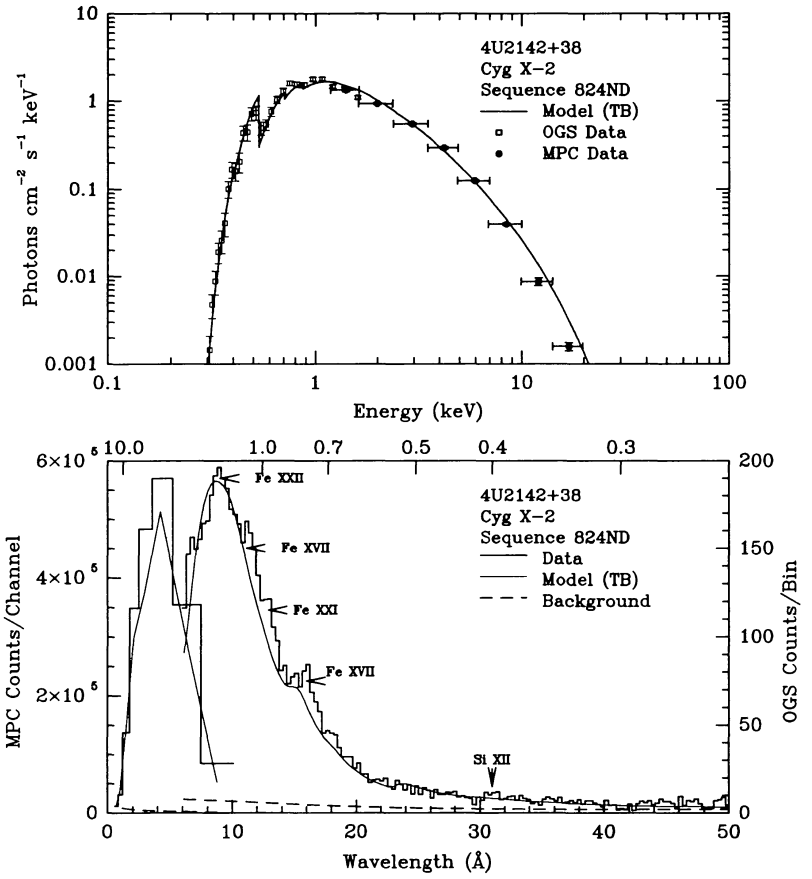

FIG. 37.—As noted in Fig. 5 for 4U 2142+38. Medium state of sequence 824.

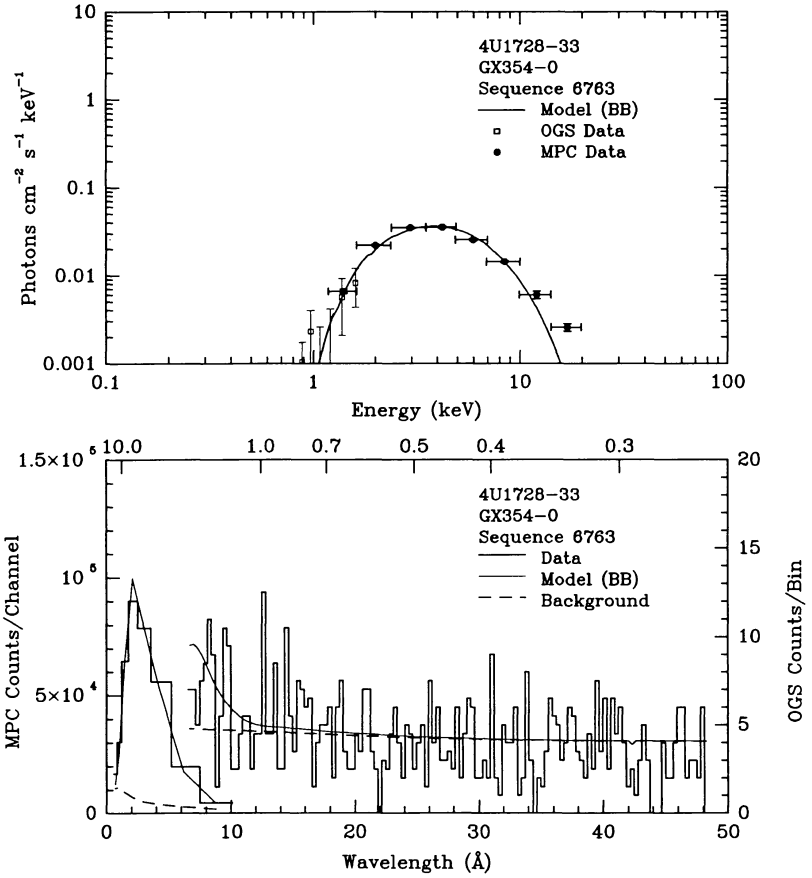

FIG. 38.—As noted in Fig. 5 for 4U 1728−33

© American Astronomical Society • Provided by the NASA Astrophysics Data System

1991ApJS...76.1127V

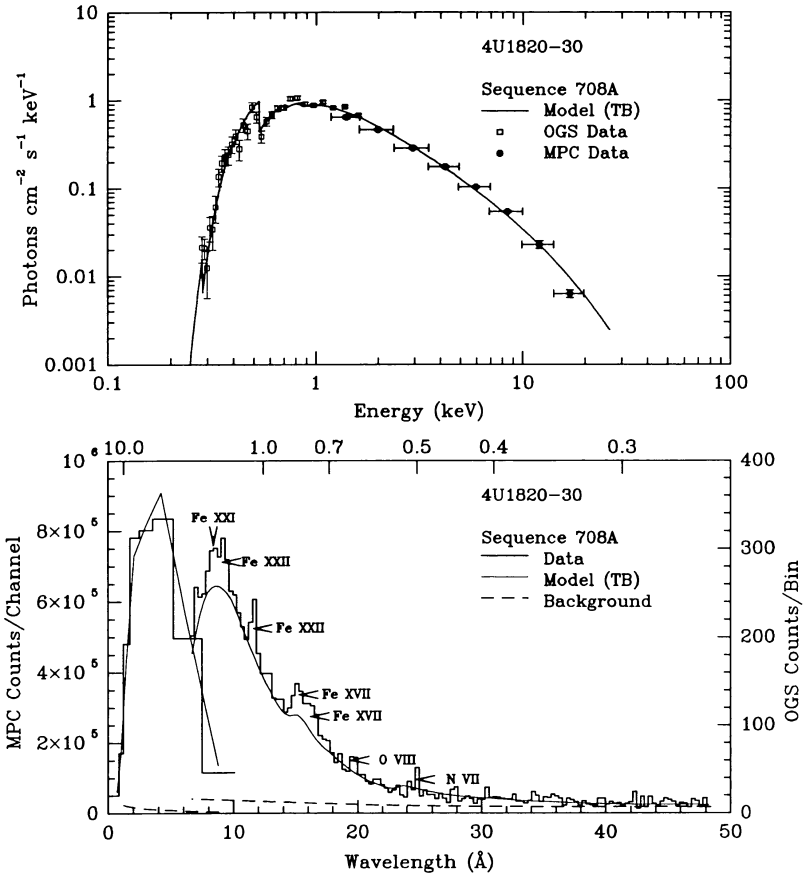

FIG. 39.—As noted in Fig. 5 for 4U 1820−30. Sequence 708A.

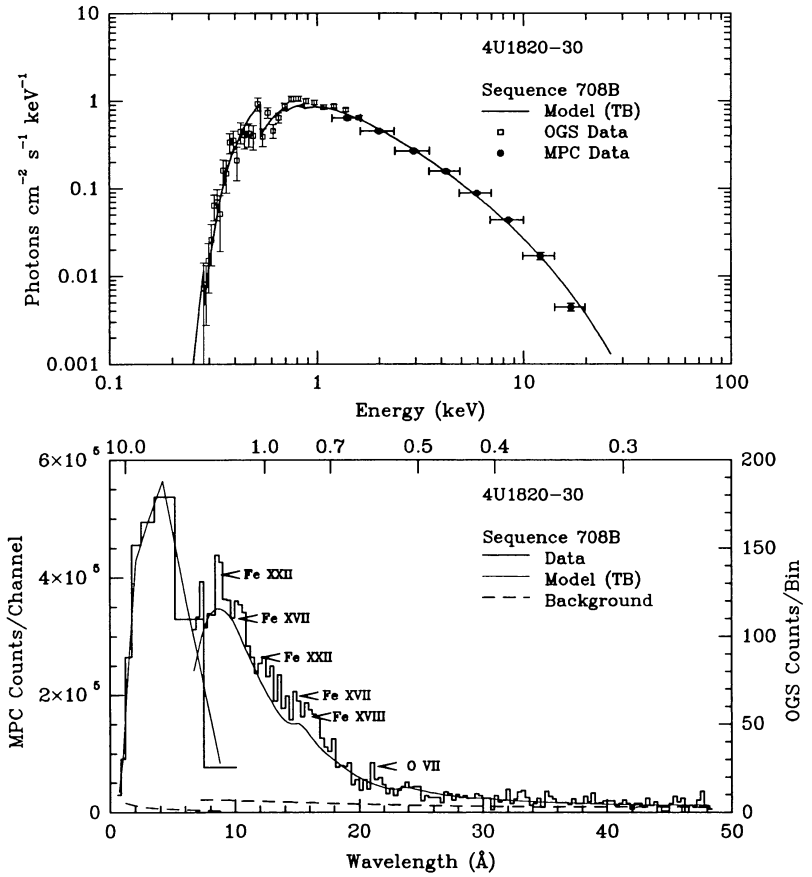

FIG. 40.—As noted in Fig. 5 for 4U 1820−30. Sequence 708B.

© American Astronomical Society • Provided by the NASA Astrophysics Data System

1991ApJS...76.1127V

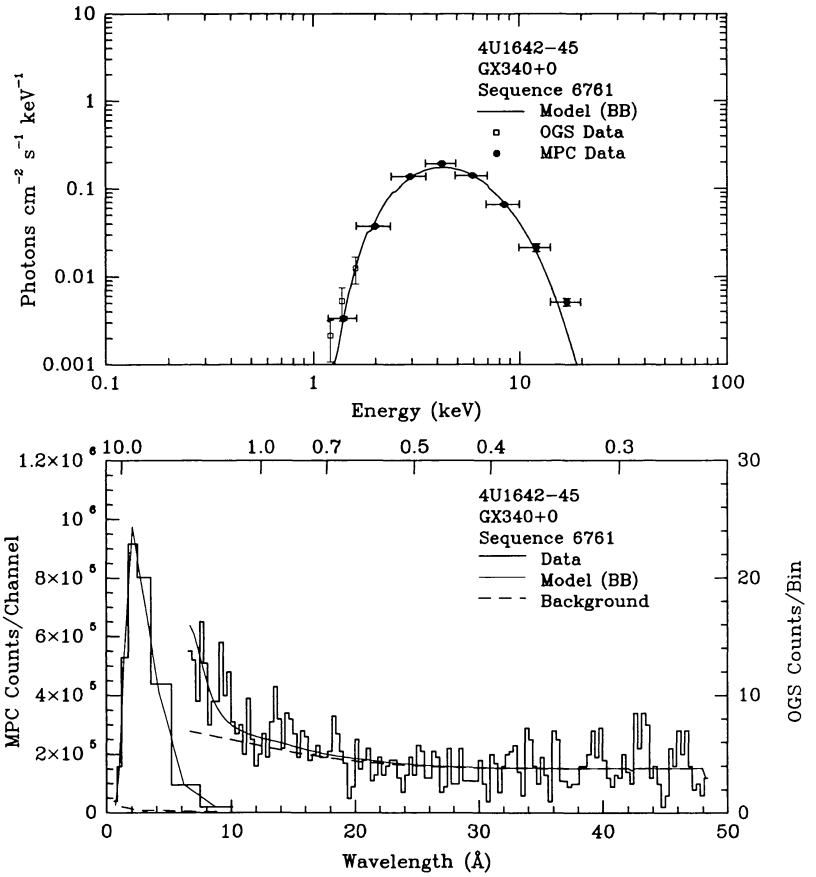

FIG. 41.—As noted in Fig. 5 for 4U 1642−45

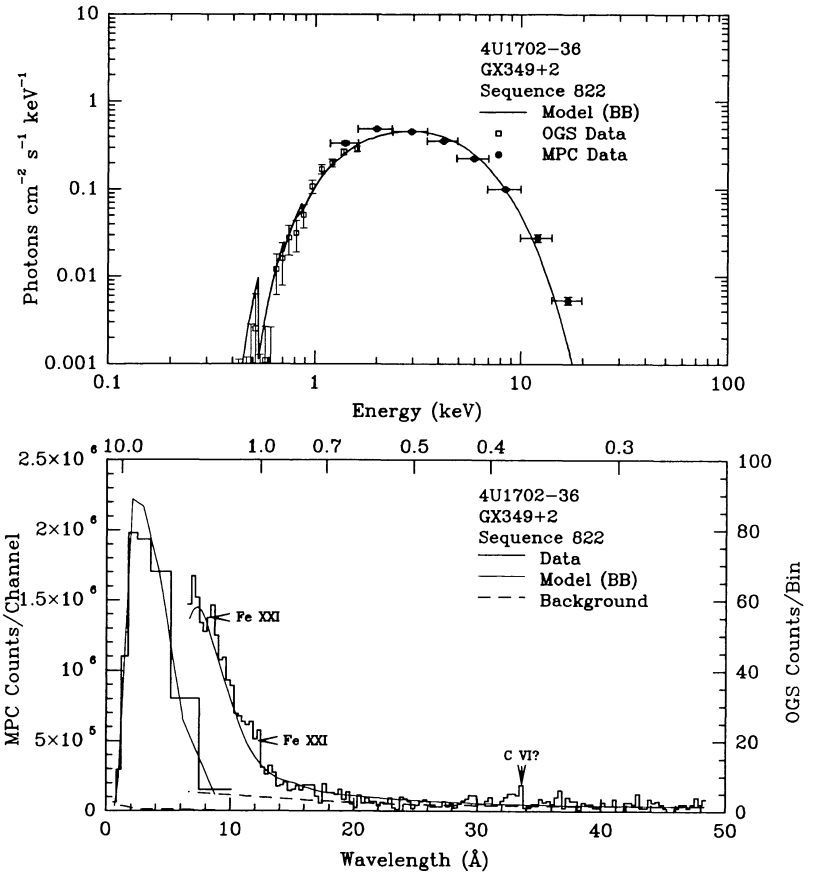

FIG. 42.—As noted in Fig. 5 for 4U 1702−36

© American Astronomical Society • Provided by the NASA Astrophysics Data System

1991ApJS...76.1127V

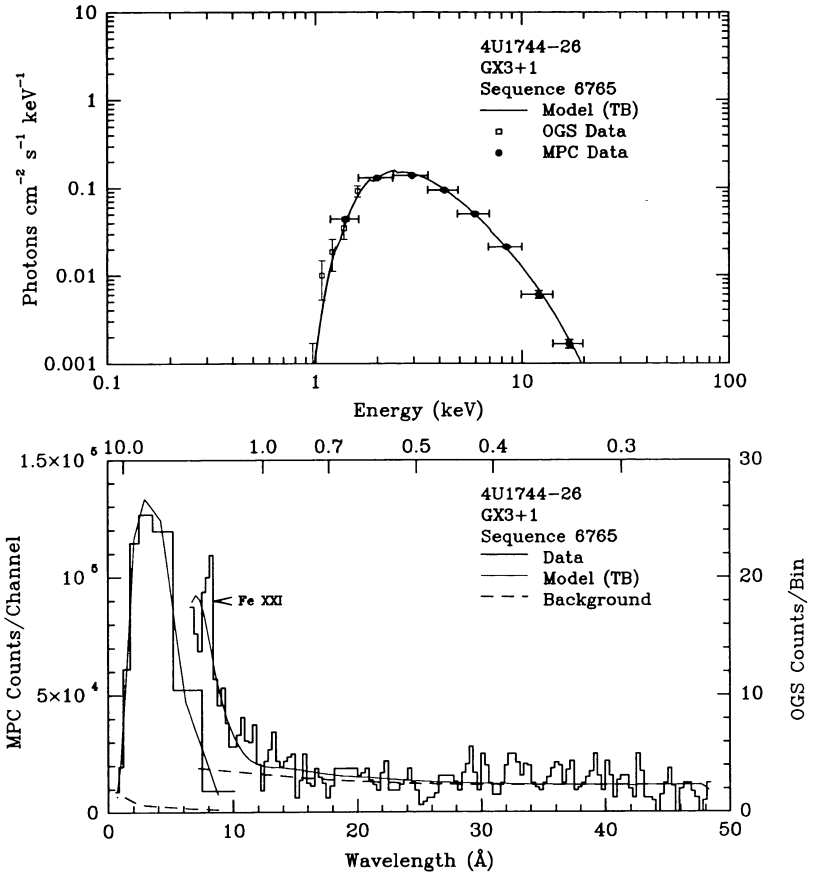

FIG. 43.—As noted in Fig. 5 for 4U 1744−26

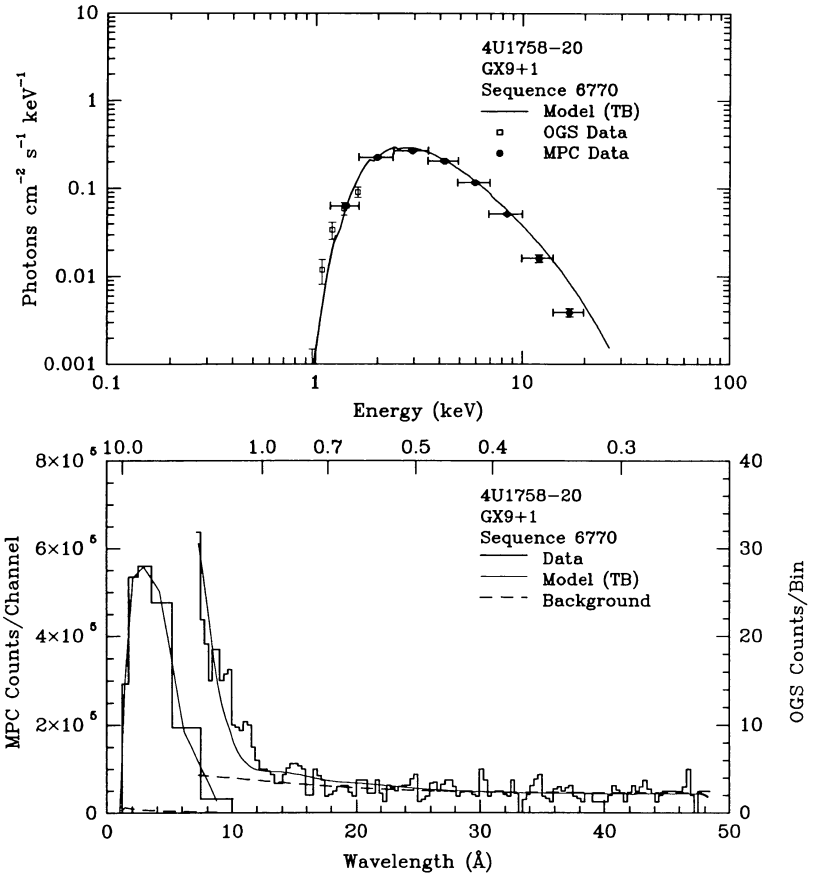

FIG. 44.—As noted in Fig. 5 for 4U 1758−20

© American Astronomical Society • Provided by the NASA Astrophysics Data System

1991ApJS...76.1127V

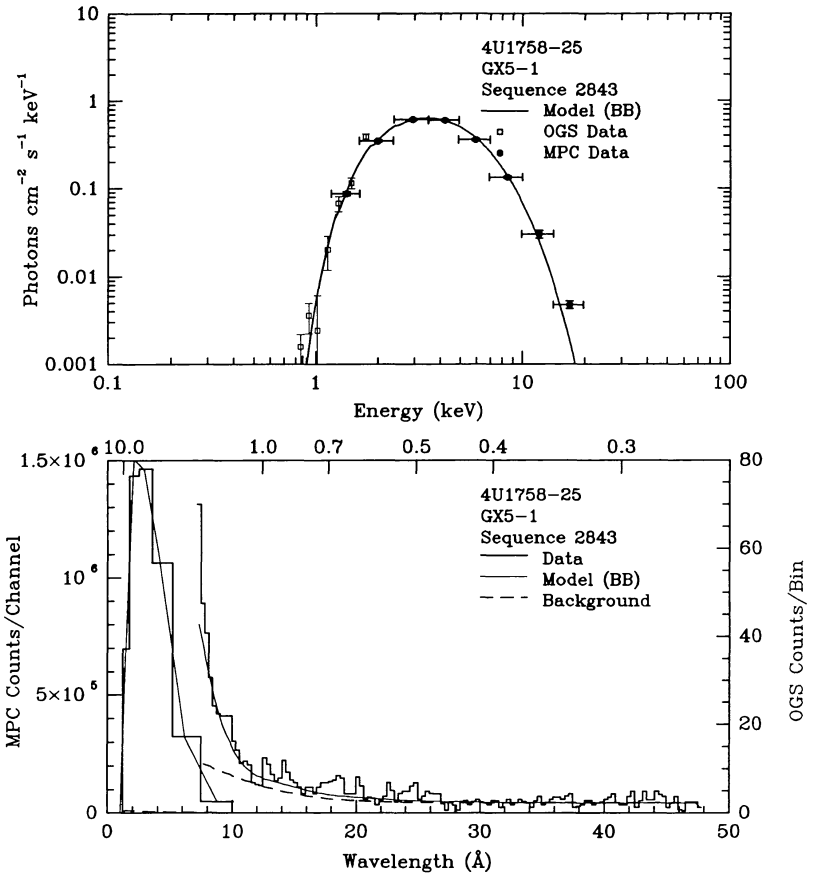

FIG. 45.—As noted in Fig. 5 for 4U 1758−25

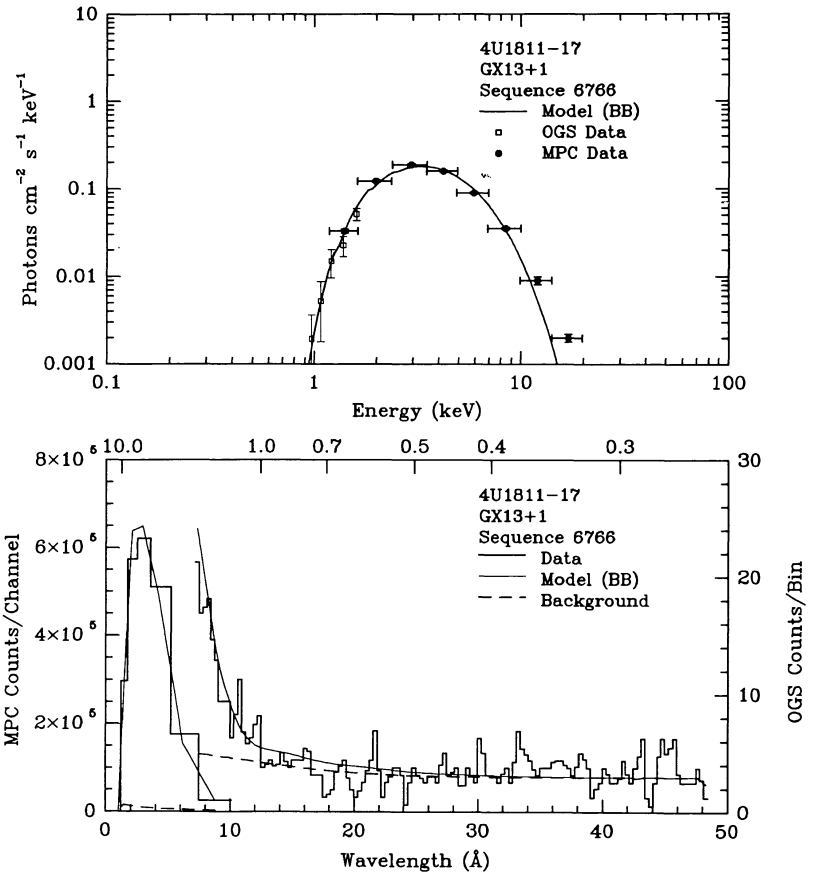

FIG. 46.—As noted in Fig. 5 for 4U 1811−17

© American Astronomical Society • Provided by the NASA Astrophysics Data System

1991ApJS...76.1127V

orbits. This observation was initially subdivided because the MPC count rate was found to vary significantly during the observation; the two subsets shown in Figures 39 and 40 represent sums of 14 (708A) and 10 (708B) binary orbits. If the lines originate in the accretion disk, one can construct geometries which cause lines to be detectable from only one part of the orbital cycle, so these features are not smeared out by integrations over the cycle. A detailed analysis, modeling the line features as a function of binary phase, will appear in Vrtilek (1991). Model fits to the SSS spectra of this source were also significantly improved when lines resolved by the OGS were included (VSK88).

4.17. *4U 1642−45 (Optically Unidentified Source GX 340+0; Figure 41)*

With a column density $N_H = 3.9 \times 10^{22}$ cm^{-2}, this source was barely detected in the OGS.

4.18. *4U 1702−36 (Optically Unidentified Source GX 349+2; Figure 42)*

Although optically unidentified, this source shows a relatively low column density ($N_H = 4.9 \times 10^{21}$ cm^{-2}) and lines attributed to Fe and C.

4.19. *4U 1744−26 (Optically Unidentified Source GX 3+1; Figure 43)*

A high column density source ($N_H = 2.9 \times 10^{22}$ cm^{-2}) showing a strong Fe XXI feature at 8 Å and excess emission between 30 and 40 Å. There are no known instrumental idiosyncracies to which we can attribute this emission. Since transmission at wavelengths greater than 30 Å is less than 10^{-4} for column densities above 10^{22} cm^{-2}, this suggests that the excess emission may be coming from a different region than the continuum emission.

4.20. *4U 1758−20 (Optically Unidentified Source GX 9+1; Figure 44)*

No significant line emission detected.

4.21. *4U 1758−25 (Optically Unidentified source GX 5−1; Figure 45)*

No significant line emission detected.

4.22. *4U 1811−17 (Optically Unidentified Source GX 13+1; Figure 46)*

No significant line emission detected.

5. DISCUSSION AND CONCLUSIONS

The combination of the high spectral resolution data of the OGS with the higher energy range data from the MPC make the X-ray column densities measured in this study the most reliable values determined to date. The extinction $A_v^{\text{X-ray}}$ implied by measured N_H is always greater than or approximately equal to optically measured A_v^{opt}. When several measurements for the same source exist, different values of X-ray column density are observed around the binary orbit; as an extreme example, the highest and lowest values we obtained (N_H = 4.0×10^{19} to 5.0×10^{23} cm^{-2}) were from different binary phases of the same source (Her X-1). These results confirm that many of the objects have a component of column density intrinsic to the source in addition to that of interstellar origin.

The K-edge absorption due to oxygen is clearly detected in 10 of the sources, and the Fe L- and Ne K-edges are detected in a few. It is likely that temperatures, densities, and geometries of the material surrounding bulge sources favor the detection of line emission over absorption edges. Since edge energies change with ionization state, edges will be broadened in the probable presence of material in several ionization states and their detection against the continuum made more difficult. The improved energy resolution of future high-energy spectrometers will be better able to distinguish different edge energies.

Although the continuum fits suggest that the massive systems favored power-law (PL) models and the low-mass systems thermal models (either bremsstrahlung [TB] or blackbody [BB]), we note that these processes do not necessarily represent the true physical processes causing the emission since other models may fit the data equally well. We therefore cannot support any specific continuum model, nor do we exclude any continuum models presented to date. Given the limitations of current data, the lack of uniqueness in model fits requires evidence independent of spectral continuum fitting before a model can be considered "true." There is no doubt that the addition of line features leads to dramatic improvement in the quality of spectral fits (Chiappetti et al. 1990; KVK89; VSK88; Makishima 1986; Brinkman et al. 1985). As the study of *Einstein* SSS observations by VSK88 showed, even instruments which cannot quite resolve the lines are influenced by their presence. We confirm VSK88's conclusion that the influence of low-energy lines must be taken into consideration for models that purport to fit the spectra of bulge sources. We can repeat for X-ray binaries the remark by Davidson & Netzer (1979) concerning the optical spectra of active galaxies: "The true continuum cannot be known until the lines are understood."

Soft X-ray line emission was detected at greater than 3 σ significance in 11 of the sources and marginally in another four. Sources from which no line emission is detected combined low signal (2–10 keV flux less than 1.5×10^{-9} ergs cm^{-2} s^{-1}) with high column densities (greater than $N_H = 2.0 \times 10^{22}$ cm^{-2}). Specific line features observed in the strongest sources (Sco X-1, Cyg X-1, and Cyg X-2) have been confirmed by *EXOSAT* TGS observations (Freeman et al. 1991; Chiappetti et al. 1990; Brinkman et al. 1985).

There is some evidence that the soft X-ray lines behave similarly to the ultraviolet lines observed from LMXBs in that for the Z-sources the line emission is enhanced during the flaring branch. The enhancement of ultraviolet line emission during the flaring states of the LMXBs has been established by recent multiwavelength observations of Cyg X-2 and Sco X-1 (Hasinger et al. 1990; Vrtilek et al. 1990, 1991). Out of the four Sco X-1 observations conducted by the OGS, only one was seen to have prominent line emission (at 11, 15, and 16 Å); the same features were seen in Sco X-1 by the *EXOSAT* TGS only during a flaring state. No prominent line features were seen in Sco X-1 during X-ray–quiescent states by the TGS. For Cygnus X-2, the line features are found to be more prominent during the flaring branch than during the normal branch.

© American Astronomical Society • Provided by the NASA Astrophysics Data System

1991ApJS...76.1127V

Possible sites for soft X-ray line emission are an X-ray–illuminated corona above the accretion disk, X-ray illumination of the inner accretion disk, and possibly the point where the accretion stream encounters the accretion disk. (In the latter case, the long exposures necessary due to the low collecting power of the OGS may have smeared out line features around the binary orbit.) It is clear that neither photoionization excitation or collisional excitation models can reproduce the relative intensities of the features. However, features that can be associated with one or the other mechanisms are observed simultaneously implying that the line emission may be from two regions: a photoionized region that is excited directly by the central source and a collisionally excited region. Since X-ray binaries are not spatially resolved, the emission originating from both coronal and photoionized regions are combined in the spectra that we have obtained.

At 1 keV the resolving power of the AXAF gratings will be 20 times that of the OGS, with an effective area 100 times greater than the OGS, and an efficiency in the first order 20 times that of the OGS (Brinkman et al. 1987; Canizares et al. 1987). The European satellite *XMM* will carry a reflection grating with a resolving power 60 times that of the OGS, and an effective area 350 times greater. These missions will result in a hitherto unobtainable combination of spectral and temporal resolution. This will enable study of the time variability of the shapes, equivalent widths, and kinematic velocities of the emission lines. The latter will constrain where in the system the line emission originates.

The authors would like to thank D. McCammon for providing the code to compute absorption cross sections for individual elements. One of the authors (S.D.V.) wishes to thank J. Trümper for hospitality at the Max-Planck-Institut für extraterrestrische Physik during the preparation of part of this paper. This work was partially supported by NASA grant NAS 8-30751 to SAO and NAG-8-494 to M.I.T.

REFERENCES

Anders, E., & Ebihara, M. 1982, Geochim. Cosmochim. Acta, 46, 2363
Arnaud, K. 1990, in preparation
Bahcall, J. N. 1978, ARA&A, 16, 241
Belloni, T., & Hasinger, G. 1990, A&A, 230, 103
Bradt, H. V. D., & McClintock, J. E. 1983, ARA&A, 21, 1 (BMC83)
Brinkman, A. C., Mewe, R., Langerwerf, T., Heise, J., Peacock, A., & White, N. 1985, Space Sci. Rev., 40, 201
Brinkman, A. C., van Rooijen, J. J., Bleeker, J. A. M., Dijkstra, J. H., Heise, J., De Korte, P. A. J., Mewe, R., & Paerels, F. 1987, Ap. Letters Comm., 26, 73
Brown, R. L., & Gould, R. J. 1970, Phys. Rev. D, 1, 2252
Canizares, C. R., et al. 1987, Ap. Letters Comm., 26, 87
Canizares, C. R., Clark, G. W., Markert, T. H., Berg, C., Smedira, M., Bardas, D., Schnopper, H., & Kalata, K. 1979, ApJ, 234, L33
Charles, P. A., Kahn, S. M., Bowyer, S., Blisset, R. J., Culhane, J. L., Cruise, A. M., & Garmire, G. 1979, ApJ, 230, L83
Chiappetti, L., et al. 1990, ApJ, 356, 591
Davidson, K., & Netzer, H. 1979, Rev. Mod. Phys., 51, 715
Dijkstra, J. H., Lantwaard, L. J., & Timmerman, C. 1978, in New Instrumentation for Space Astronomy, ed. K. A. van der Hucht & G. S. Vaiana (London: Pergamon), 257
Doschek, G. A., & Cowan, R. D. 1984, E. O. Hulbert Center for Space Research preprint
Freeman, P., Kahn, S. M., & Vrtilek, S. D. 1991, in preparation
Gaillarditz, R., et al. 1979, IEEE Trans. Nucl. Sci., 25, 437
Gorenstein, P. 1975, ApJ, 198, 95
Grindlay, J. E., et al. 1980, ApJ, 240, L121
Halpern, J. P. 1982, Ph.D. thesis, Harvard University
Hasinger, G., et al. 1985, Nature, 319, 469
Hasinger, G., van der Klis, M., Ebisawa, K., Dotani, T., & Mitsuda, K. 1990, A&A, 235, 131
Heiles, C., Stark, A. A., & Kulkarni, S. 1981, ApJ, 247, L73
Henke, B. L., Lee, P., Tanaka, T. J., Shimabukuro, R. L., & Fujikawa, B. K. 1982, Atomic Data Nucl Data Tables, 27, 1
Henry, J. P., et al. 1977, Proc. Soc. Photo Optical Inst. Eng., 106, 196
Kahn, S. M., & Blisset, R. J. 1980, ApJ, 238, 417
Kahn, S. M., & Seward, F. D. 1982, unpublished
Kahn, S. M., Seward, F. D., & Chlebowski, T. 1984, ApJ, 283, 286 (KSC84)
Kallman, T. R., & McCray, R. 1982, ApJS, 50, 263
Kallman, T. R., Vrtilek, S. D., & Kahn, S. M. 1989, ApJ, 345, 498 (KVK89)
Kallman, T. R., Vrtilek, S. D., Raymond, J. C., Smith, B., & Kahn, S. M. 1991, in preparation
Kato, T. 1976, ApJS, 30, 397
Kellogg, E., Baldwin, J. R., & Koch, D. 1975, ApJ, 199, 299
Lamb, F. K. 1989, in Fourteenth Texas Symposium on Relativistic Astrophysics (Ann. NY Acad. Sci., 571, 347)
Lewin, W. H. G., & Joss, P. C. 1983, in Accretion Driven Stellar X-ray Sources, ed. W. H. G. Lewin & E. P. J. van den Heuvel (Cambridge: Cambridge Univ. Press), 41
Liedahl, D. A., Kahn, S. M., Osterheld, A. L., & Goldstein, W. H. 1990, ApJ, 350, L37
Lockman, F. J., Jahoda, K., & McCammon, D. 1986, ApJ, 302, 432
Makishima, K. 1986, in The Physics of Accretion onto Compact Objects, ed. K. O. Mason, M. K. Watson, & N. E. White (Berlin: Springer), 249
Mason, K. O. 1986, in The Physics of Accretion onto Compact Objects, ed. K. O. Mason, M. K. Watson, & N. E. White (Berlin: Springer), 29
McClintock, J. E., London, R. A., Bond, H. E., & Grauer, A. D. 1982, ApJ, 258, 245
McCray, R. A., Shull, J. M., Boynton, P. E., Deeter, J. E., Holt, S. S., & White, N. E. 1982, ApJ, 262, 301
Mewe, R., et al. 1982, ApJ, 260, 233
Morrison, R., & McCammon, D. 1983, ApJ, 270, 119 (MM83)
Osborne, J., et al. 1986, MNRAS, 221, 823
Ponman, T. J., Foster, A. J., & Ross, R. R. 1990, MNRAS, 246, 287 (PFR90)
Pravdo, S. H., White, N. E., Kondo, Y., Becker, R. H., Boldt, E. A., Holt, S. S., Serlemitsos, P. J., & McCluskey, G. E. 1980, ApJ, 237, 71
Rappaport, S. A., & Joss, P. C. 1983, in Accretion-Driven Stellar X-ray Sources, ed. W. H. G. Lewin & P. J. van den Heuvel (Cambridge: Cambridge Univ. Press), 1
Raymond, J. C., & Smith, B. H. 1977, ApJS, 35, 419
Ruderman, M., Shaham, J., Tavani, M., & Eichler, D. 1989, ApJ, 343, 292
Schreier, E., Levinson, R., Gursky, H., Kellogg, E., Tananbaum, H., & Giacconi, R. 1972, ApJ, 172, 79
Seward, F., et al. 1982, Appl. Optics, 21, 2012 (S82)
Stella, L., Priedhorsky, W. C., & White, N. E. 1987, ApJ, 312, L17
Tananbaum, H., Gursky, H., Kellogg, E., Levinson, R., Schreier, E., & Giacconi, R. 1972, ApJ, 174, 143
Toor, A., & Seward, F. D. 1974, ApJ, 79, 995
Vacca, W. D., Sztajno, M., Lewin, W. H. G., Trümper, J., van Paradijs, J., & Smith, A. 1987, A&A, 172, 143
van der Klis, M., et al. 1985, Nature, 316, 225
Vrtilek, S. D. 1991, in preparation
Vrtilek, S. D., & Halpern, J. H. 1985, ApJ, 296, 606
Vrtilek, S. D., Helfand, D. J., Halpern, J. H., Kahn, S. M., & Seward, F. D. 1986a, ApJ, 308, 644 (Vrt86a)
Vrtilek, S. D., Kahn, S. M., Grindlay, J. E., Helfand, D. J., & Seward, F. D. 1986b, ApJ, 307, 698 (Vrt86b)
Vrtilek, S. D., Penninx, W., Raymond, J. C., Verbunt, F., Hertz, P., Wood, K., Lewin, W. H. G., & Mitsuda, K. 1991, ApJ, in press
Vrtilek, S. D., Raymond, J. C., Garcia, M., Verbunt, F., Hasinger, G., & Kürster, M. 1990, A&A, 235, 162
Vrtilek, S. D., Swank, J. H., & Kallman, T. R. 1988, ApJ, 326, 186 (VSK88)
Wiese, W. L. 1985, ed. Atomic Data for Fusion, IV (Oak Ridge: Controlled Fusion Atomic Data Center)

© American Astronomical Society • Provided by the NASA Astrophysics Data System